Research Article | Open Access

Microstructures

Zha et al. Microstructures 2026, 6, 20260111 DOI:10.20517/microstructures.2026.114

Tuning hydride stability in TiVZrNb high-entropy hydrogen storage alloys via alloy-hydrogen electronegativity difference

Liangliang Zha[1,2], Liyuan Liu[3], Yihang Wang[1,2,3], Hongmei Cai[1,2], Yakun Zhang[1,2], Huijie Du[1,2,3], Bang Dou[2], Lufeng Xue[2], Yumeng Zhao[2], Di Wan[2,3], Yunfei Xue[1,2]

Keywords:
TiVZrNb-based alloy, dehydrogenation thermodynamics, average electronegativity difference, desorption enthalpy, apparent activation energy

Citation: Zha, L.; Liu, L.; Wang, Y.; Cai, H.; Zhang, Y.; Du, H.; Dou, B.; Xue, L.; Zhao, Y.; Wan, D.; Xue, Y. Tuning hydride stability in TiVZrNb high-entropy hydrogen storage alloys via alloy-hydrogen electronegativity difference. *Microstructures* **2026**, *6*, 20260111. https://dx.doi.org/10.20517/microstructures.2026.114

Received: 25 May 2026 **First Decision:** 22 Jun 2026 **Revised:** 5 Jul 2026 **Accepted:** 23 Jul 2026 **Published:** 25 Aug 2026

Academic Editor: Tao Yang
Copy Editor: Shu-Yuan Duan
Production Editor: Shu-Yuan Duan

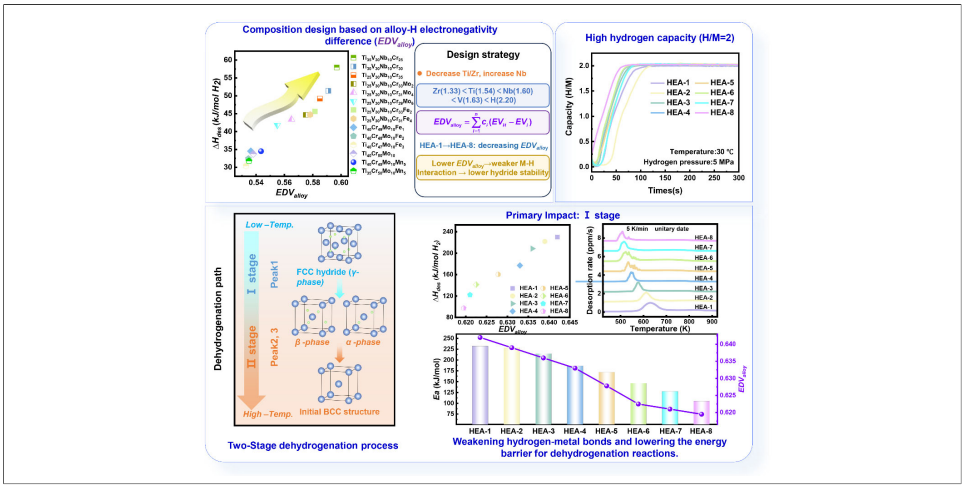

Abstract

TiVZrNb-based body-centered cubic (BCC) hydrogen-storage high-entropy alloys (HEAs) possess high hydrogen storage capacity. However, the high thermodynamic stability of their hydrides results in elevated dehydrogenation temperatures, limiting their practical applications. Microstructural parameter tuning offers a powerful route to optimize hydrogen storage behavior. To achieve effective thermodynamic control of hydrogen desorption, this study, based on statistical analysis of previous data on single-phase BCC hydrogen storage HEAs, found that compared to valence electron concentration (*VEC*), lattice constants, and lattice distortion (δ), the average electronegativity difference between the alloy and hydrogen (EDV_{alloy}) exhibits a clearer positive correlation with desorption enthalpy (ΔH_{des}). Based on this, the HEA-1 to HEA-8 series of hydrogen storage alloys were designed using EDV_{alloy} as the compositional parameter for thermodynamic control of hydrogen desorption. The results show that all alloys exhibit a single-phase BCC structure and maintain a high hydrogen storage capacity (H/M = 2). As the EDV_{alloy} of the

[1]School of Materials Science and Engineering, Beijing Institute of Technology, Beijing 100081, China.
[2]Yangtze Delta Region Academy of Beijing Institute of Technology, Jiaxing 314019, Zhejiang, China.
[3]School of Interdisciplinary Sciences, Beijing Institute of Technology, Beijing 100081, China.

Correspondence to: Prof. Di Wan, School of Interdisciplinary Sciences, Beijing Institute of Technology, Beijing 100081, China; Yangtze Delta Region Academy of Beijing Institute of Technology, Jiaxing 314019, Zhejiang, China. E-mail: diwan@bit.edu.cn. Prof. Yunfei Xue, School of Materials Science and Engineering, Beijing Institute of Technology, Beijing 100081, China; Yangtze Delta Region Academy of Beijing Institute of Technology, Jiaxing 314019, Zhejiang, China. E-mail: xueyunfei@bit.edu.cn

alloys decreased from 0.6420 to 0.6195, ΔH_{des} decreased from 230.3 kJ/mol H_2 to 97.3 kJ/mol H_2, indicating a significant reduction in the thermodynamic stability of the hydride. Thermal desorption spectroscopy (TDS) analysis further revealed that the reduction in EDV_{alloy} shifts the main dehydrogenation peak toward lower temperatures and lowers the apparent activation energy (E_a) for the decomposition of hydrogen-rich dihydrides. The results confirm the feasibility of using EDV_{alloy} to control the thermodynamic parameters of hydrogen release in single-phase BCC hydrogen-storage HEAs and provide a viable approach for designing low-temperature hydrogen-releasing high-entropy hydrogen-storage alloys.

INTRODUCTION

Due to its high energy density, clean nature, and wide availability, hydrogen is considered one of the key enablers of the transition to a low-carbon energy system[1-3]. However, hydrogen is highly flammable and has a low volumetric density at room temperature and standard pressure, making safe and efficient hydrogen storage and transportation technologies critical challenges to its widespread adoption[4,5]. Compared to high-pressure gaseous and cryogenic liquid hydrogen storage, metal hydride hydrogen storage offers advantages such as high volumetric hydrogen storage density, good safety, and reversible hydrogen absorption and desorption, making it a subject of widespread attention in the field of solid-state hydrogen storage[6]. Compared to traditional hydrogen storage alloys, hydrogen-storage high-entropy alloys (HEAs) possess high configurational entropy and a broad range of compositional control, providing new insights into metal hydride hydrogen storage materials[7,8]. Among these, BCC hydrogen-storage HEAs, due to their lattice chemical disorder and diverse local chemical environments, can provide abundant tetrahedral and octahedral voids for hydrogen atoms, thereby offering the potential for higher hydrogen storage capacities than traditional BCC alloys[9-11]. Consequently, BCC high-entropy hydrogen storage alloys are considered a significant research direction for high-capacity solid-state hydrogen storage materials.

The TiVZrNb-based BCC HEA is a typical high-capacity hydrogen-storage alloy system[12]. All elements in this system are strong hydride-forming elements that readily form a body-centered cubic (BCC) solid solution structure. After hydrogen absorption, they can form hydrogen-rich hydrides with a hydrogen-to-metal atom ratio (H/M) approaching 2, thereby exhibiting a high theoretical hydrogen storage capacity[13-15]. At the same time, the elemental composition of this system can be continuously adjusted over a wide range, providing an excellent platform for studying the relationships between alloy composition, phase structure, and hydride stability. For example, the multi-component alloy $Ti_{0.325}V_{0.275}Zr_{0.125}Nb_{0.275}$ reported by Montero *et al.*[16] can form a single-phase BCC structure and exhibits reversible hydrogen absorption and desorption behavior, demonstrating that the TiVZrNb system has good potential for hydrogen storage applications. However, while strong metal-hydrogen interactions endow the alloy with high hydrogen absorption capacity, they also lead to excessive thermodynamic stability of the hydrides, manifested as a high desorption enthalpy, a low plateau pressure, and a high desorption temperature[17-19]. This issue limits the practical application of TiVZrNb-based BCC hydrogen-storage HEAs for reversible hydrogen storage at low and medium temperatures. Therefore, effectively regulating the thermodynamic stability of hydrides while maintaining a single-phase BCC structure and high hydrogen storage capacity is a key issue in the composition design of this system.

Currently, semi-empirical parameters of some HEAs, such as VEC[20], lattice constants[21], and δ[22], are closely related to their hydrogen storage performance. Among these, VEC is commonly used to assess the tendency for phase formation[23,24]; the atomic size difference reflects the ability to form a solid solution and the degree of lattice distortion[25,26]. Lattice constants are closely related to interstitial size and the space occupied by hydrogen[21,27]. Somo *et al.*[28] reported that the hydrogen storage performance of BCC-structured hydrogen storage alloys shows a relatively weak correlation with atomic size difference but exhibits a certain degree of

correlation with the alloy's VEC. Nygård *et al.*[20] proposed that the hydride stability of high-entropy alloys can be regulated via VEC, providing an important basis for designing the electron concentration of hydrogen-storage HEAs. Furthermore, Jiang *et al.*[29] proposed that hydrogen affinity (ΔH_{aff}) can serve as a physical descriptor for high-entropy hydrogen storage alloys. They demonstrated that it correlates well with the hydrogen binding energy, hydride formation enthalpy, and dehydrogenation temperature of BCC high-entropy alloys. However, these parameters mainly describe hydrogen storage behavior from the aspects of average electron concentration, lattice geometry, and atomic-size mismatch, and their ability to directly describe the thermodynamic stability of hydrides is still limited. Specifically, VEC mainly reflects the overall electron concentration and phase-forming tendency of the alloy, but it cannot directly describe the strength of metal-hydrogen bonding. The δ and lattice constants can reflect lattice distortion and the available interstitial space for hydrogen atoms, but they do not directly characterize the electronic interaction and charge-transfer tendency between alloy elements and hydrogen. Therefore, although these parameters are useful for alloy design, it remains difficult to use them alone to directly evaluate hydride stability and hydrogen desorption thermodynamics. Recently, Zhai *et al.*[21] summarized the research progress on BCC hydrogen storage alloys, concluding that electronegativity is a key factor influencing hydrogen storage performance, with the electronegativity difference serving as a measure of the strength of interactions between alloy elements and hydrogen. Since charge transfer during hydrogen absorption primarily occurs between alloy elements and H atoms, the EDV_{alloy} serves as a key indicator for understanding the alloy's hydrogen storage behavior[30,31]. However, research on systematically regulating the thermodynamic stability of hydrides in BCC hydrogen storage HEAs based on the EDV_{alloy} remains relatively limited. Therefore, understanding the influence of the electronegativity difference on hydride stability is of great significance for guiding the design of hydrogen storage alloys.

This paper first compiles data on previously reported single-phase BCC hydrogen storage HEAs and compares the relationships between EDV_{alloy}, VEC, lattice parameters, and δ with the enthalpy of ΔH_{des} to identify compositional descriptors that more effectively reflect thermodynamic trends in hydrogen desorption. The results indicate that EDV_{alloy} exhibits a clearer positive correlation with ΔH_{des}. Based on these findings, the HEA-1 to HEA-8 series of hydrogen storage alloys were designed and prepared using EDV_{alloy} as the thermodynamic control parameter for hydrogen desorption. All these alloys exhibit a single-phase BCC structure and maintain a high hydrogen storage capacity (H/M = 2). A decrease in EDV_{alloy} weakens the metal-hydrogen bond while simultaneously lowering the E_a of the dihydride decomposition, thereby reducing the hydride's stability. Based on these findings, the feasibility of using EDV_{alloy} to regulate the thermodynamic parameters of hydrogen release in single-phase BCC high-entropy hydrogen storage alloys was confirmed, providing valuable guidance for the design of low and medium-temperature high-entropy hydrogen storage alloys.

EXPERIMENTAL

Sample preparation

The raw materials selected for this work (Ti, V, Zr, Nb) were small metal ingots, each with a purity better than 99.99 wt.% and purchased from Hebei Ancai New Material Technology Co., Ltd., China. Under an argon-protected atmosphere (99.999%, Linde Gas, China), a series of alloys with different compositions was prepared using the non-consumable vacuum arc melting method (SKY08K-102, Shenyang Scientific Instrument Research Center Co., Ltd., Chinese Academy of Sciences, China). To ensure compositional homogeneity, each ingot underwent at least four cycles of inversion and remelting. Subsequently, the as-cast alloy ingots were vacuum-sealed in quartz tubes, annealed at 1473 K for 2 h, and then water-quenched to obtain a uniform microstructure. The alloys are designated as HEA-1 to HEA-8 in descending order of their electronegativity difference. The physical parameters of the elements used in the calculations in this paper are shown in Supplementary Table 1[32].

Microstructural characterization

The heat-treated samples were cut into 5 mm × 5 mm × 3 mm specimens, and the test surfaces were polished with sandpaper to remove the oxide layer. The crystal structure and lattice parameters of the alloy were analyzed using an X-ray diffractometer (Rigaku SmartLab SE, Cu Kα radiation, Japan) with a 2θ range of 20-90°. These XRD patterns were mainly used for phase identification and comparison of the overall phase constitution. For lattice-constant refinement of HEA-1 to HEA-8, additional XRD patterns were collected at a slower scan rate of 2°/min. The diffraction data collected at 2°/min were refined using GSAS-II software with Rietveld refinement, incorporating instrument parameters, lattice constants, and preferred orientations. The XRD patterns of the hydrogenated samples with different hydrogen contents were also collected at a scan rate of 2°/min. To further characterize the microstructure and composition distribution, the heat-treated specimens were hot-embedded and polished to a mirror finish. Subsequently, observation and analysis were performed using a scanning electron microscope (Sigma 300 Carl Zeiss Microscopy GmbH, Germany) equipped with an energy-dispersive spectrometer (EDS, Oxford Instruments, United Kingdom). Imaging employed a backscattered electron (BSE) detector at 20 kV acceleration voltage, 15 spot size, and 10 mm working distance to clearly reveal grains and grain boundaries.

Hydrogen storage measurements

The heat-treated samples were cut into 4 mm × 4 mm × 4 mm specimens and polished with sandpaper to remove the oxide layer, preparing them for subsequent hydrogen storage performance testing. High-purity H_2 gas (99.999%, Linde Gas, China) was used for all hydrogen absorption/desorption and pressure-composition isotherm (PCT) measurements. Alloy activation, hydrogen absorption/desorption kinetics, and PCT tests were conducted using a fully automated Sieverts-type apparatus (H2PCT-22101, GASTOUCH, Yangzhou University, China). The hydrogen uptake/release amount was calculated from the pressure-volume-temperature data obtained using the Sieverts-type apparatus. To improve the accuracy of the hydrogen capacity calculation, the system's dead volume was calibrated before measurement, and the amount of hydrogen gas was calculated using the real-gas equation $n = PV/(ZRT)$, where Z is the compressibility factor of hydrogen at the corresponding temperature and pressure. The specific experimental procedure is as follows: First, approximately 1.0 g of alloy sample was used for each PCT measurement. The sample was weighed and dynamically evacuated at 673 K for 2 h under a dynamic vacuum level of 10^{-4} MPa (approximately 100 Pa) for activation. After cooling to 303 K, the initial hydrogen-uptake kinetics test was conducted at 5 MPa hydrogen pressure. Following hydrogen uptake, the sample was heated to 773 K for high-temperature dehydrogenation to prepare for subsequent PCT testing at different temperatures. To eliminate residual hydrogen effects on test results, the high-temperature dehydrogenation step was repeated before each PCT test. Due to significant variations in plateau pressure among different alloy samples and the difficulty of hydrogen desorption below 0.001 MPa, the PCT test temperature was controlled to maintain the hydrogen absorption/desorption plateau pressure within approximately 0.001-10 MPa for each sample, ensuring a complete PCT curve (actual test temperature was determined by the plateau region temperature due to potential fluctuations during testing). Additionally, a thermal desorption spectrometer (TDS: G8 GALILEO, Bruker, AXS GmbH, Germany) was used to perform programmed-temperature desorption tests on samples after the initial hydrogen-uptake kinetics. For each TDS measurement, approximately 0.1 g of hydrogenated sample was used according to the standard sample-mass requirement of the instrument. The heating rates were set at 5 K/min, 10 K/min, 15 K/min, and 20 K/min to analyze their hydrogen desorption behavior.

RESULTS

Alloy composition design based on the control of the electronegativity difference

The primary issue facing TiVZrNb-based hydrogen-storage HEAs is excessively high hydrogen-release temperatures, a problem fundamentally caused by the alloy's hydrides' high stability[33]. Therefore, effectively regulating the thermodynamic behavior of hydrogen release is crucial for the practical application of these

alloys. In hydrogen-storage HEAs, the equilibrium pressure for hydrogen absorption and desorption is a key parameter that describes the thermodynamic properties of hydrogen desorption. It is typically obtained by testing PCT curves at different temperatures. At a given temperature, a higher equilibrium pressure for hydrogen absorption and desorption indicates that the alloy is more difficult to hydrate and that the hydride is more prone to decomposition. However, for alloys with significant differences in hydrogen release thermodynamics, it is difficult to directly compare equilibrium pressures at the same temperature. Therefore, the relationship between temperature and decomposition pressure is typically derived by fitting the Van't Hoff equation to equilibrium pressure data at different temperatures, which is then used to calculate the reaction entropy and enthalpy of hydride formation[34]. The Van't Hoff equation is given in[22]:

$$\ln P = \frac{\Delta H}{RT} - \frac{\Delta S}{R} \tag{1}$$

where P is the equilibrium pressure for hydrogen absorption/desorption, T is the test temperature, R is the ideal gas constant [8.314 J/(mol·K)], and ΔS and ΔH are the reaction entropy and reaction enthalpy of the corresponding hydrogen absorption or desorption process, respectively. A larger absolute value of ΔH indicates that the hydride is more stable and that the energy required for dehydrogenation is higher. Therefore, ΔH can accurately reflect the thermodynamic performance of the alloy during hydrogen desorption. However, determining ΔH typically relies on lengthy PCT testing or complex theoretical calculations. Therefore, it is necessary to identify empirical parameters that predict thermodynamic trends in hydrogen release as a function of alloy composition to guide the design of hydrogen-storage HEAs with a BCC structure.

Previous studies have shown that several key parameters of high-entropy alloys, such as electronegativity difference[21], VEC[35], lattice constants[21], and lattice distortion (δ)[36], are closely related to their thermodynamic properties of hydrogen release. Among these, the average electronegativity difference between the alloy and hydrogen can be used to describe the average electronic interaction between them. EDV_{alloy} can be calculated using[21]:

$$EDV_{\text{alloy}} = \sum_{i=1}^{n} c_i \left(EV_H - EV_i\right) \tag{2}$$

where c_i is the concentration of element i in the alloy, and EV_i and EV_H are the Pauling electronegativities of element i and hydrogen, respectively. Since the electronegativities of the elements in this study are all lower than that of hydrogen, a larger EDV_{alloy} value indicates a greater average electronegativity difference between the alloy and hydrogen. VEC is the average valence electron count of each element, calculated as follows[35]:

$$VEC = \sum_{i=1}^{n} c_i (VEC)_i \tag{3}$$

The lattice distortion (δ) is calculated as given in[36]:

$$\delta = \sqrt{\sum_{i=1}^{n} c_i \left(1 - r_i/\bar{r}\right)^2} \times 100\%, \bar{r} = \sum_{i=1}^{n} c_i r_i \tag{4}$$

where r_i is the atomic radius of element i, and is the average atomic radius. To investigate the relationship between the above parameters and the thermodynamics of hydrogen release, this section performs a statistical analysis of 14 hydrogen-storage HEAs previously reported by our research group. The selection criteria are as follows: (1) The alloy must have a single-phase BCC structure to eliminate the interference of multi-phase structures on the thermodynamics of hydrogen release; (2) Alloys previously reported by our research group were selected to ensure consistency in preparation processes and testing conditions, thereby reducing the impact of experimental errors on the correlation of parameters.

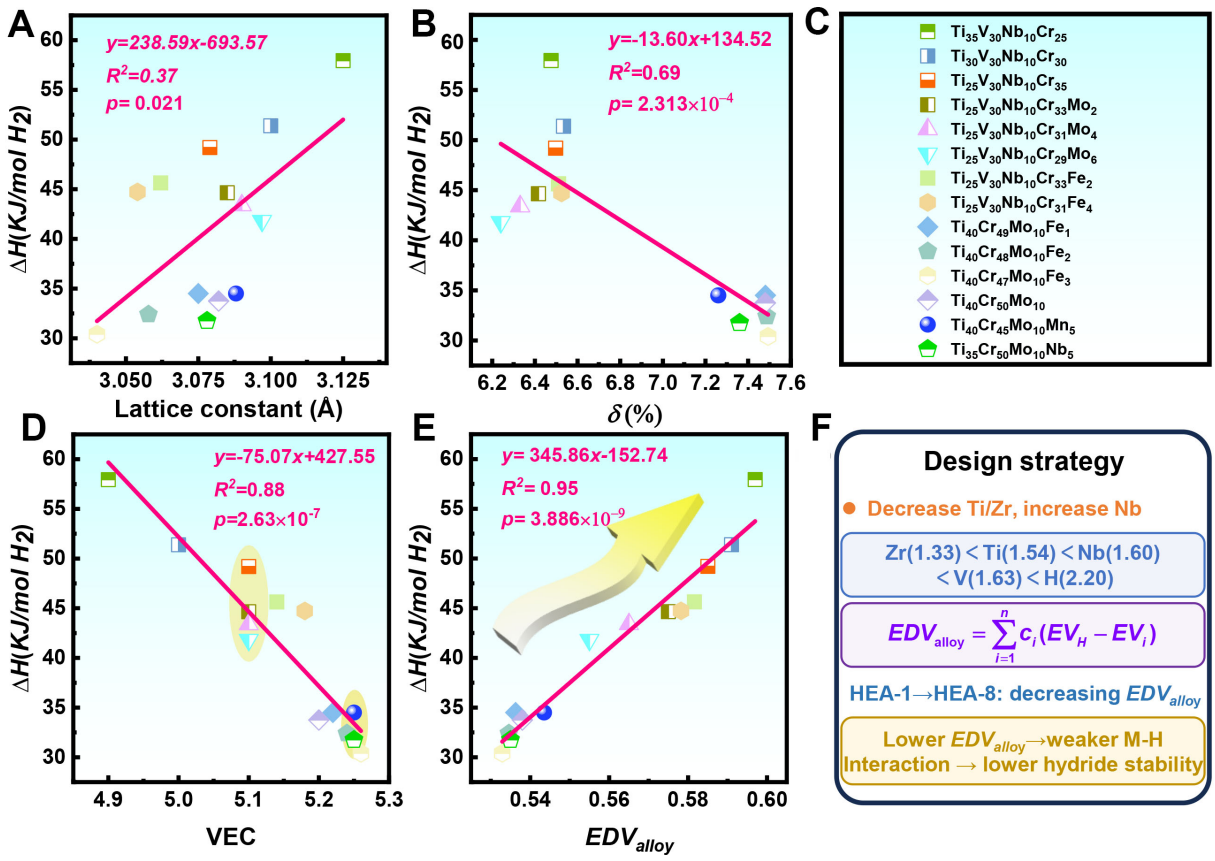

Figure 1. Correlation between the ΔH_{des} of single-phase BCC alloys reported in the literature and (A) lattice constants, (B) δ, (C) corresponding alloy composition; (D) *VEC*, and (E) EDV_{alloy}; (F) design strategy. The linear fitting results, including R^2 and *P-values*, are shown in the corresponding panels. VEC: Valence electron concentration; ΔH_{des}: desorption enthalpy; EDV_{alloy}: electronegativity difference value of the alloy; HEA: high-entropy alloy; δ: lattice distortion; BCC: body-centered cubic.

Based on the above selection criteria, the compiled data were plotted with the key parameters on the x-axis and the thermodynamic parameter ΔH_{des} on the y-axis. Linear fitting was then performed to quantitatively assess the correlations between different descriptors and ΔH_{des}; the results are shown in Figure 1. In Figure 1A, no clear pattern is observed in the variation of ΔH_{des} with lattice parameters. Figure 1B shows that lattice distortion exhibits a relatively weak correlation with ΔH_{des} compared with *VEC* and EDV_{alloy}. This indicates that lattice parameters or lattice distortion cannot accurately describe the thermodynamic changes in hydrogen release for these alloys. Figure 1D shows that ΔH_{des} decreases with increasing VEC. This suggests that a higher *VEC* reduces hydride stability to some extent, a trend consistent with the findings of Nygård *et al.*[20]. However, for some alloys, such as 3, 6, 7, and 8, the VEC values are all 5.1, yet the measured ΔH_{des} values differ significantly; similarly, alloys 9 and 13 both have a VEC of 5.25, yet their ΔH_{des} values differ. This indicates that a single global *VEC* parameter is insufficient to fully describe the thermodynamic differences in hydrogen release among alloys. This is because *VEC* is essentially the component-weighted average of the total valence-electron counts of the alloy's elements, primarily reflecting the alloy's overall average electron concentration. For hydrogen storage HEAs, even if different alloys have the same or similar global *VEC* values, their local chemical environments and d-orbital distributions may still differ significantly. Particularly in transition metal hydrides, the hybridization between the H 1s state and the metal d states has a significant impact on the M-H bond strength. In contrast, the global *VEC* struggles to distinguish the contributions of localized d states from different elements to hydrogen-occupancy stability[21,29,37]. Therefore, relying solely on the global *VEC* makes it difficult to accurately describe the thermodynamics of hydrogen release in alloys.

Table 1. The composition, phase structure, EDV_{alloy}, VEC, δ, and ΔH_{des} of the alloys reported in the literature

Alloy	Composition (as reported)	Phase	EDV_{alloy}	VEC	a (Å)	δ (%)	ΔH_{des} [kJ/mol H_2]	Ref.
1	$Ti_{35}V_{30}Nb_{10}Cr_{25}$	BCC	0.597	4.90	3.125	6.476	57.94	[41]
2	$Ti_{30}V_{30}Nb_{10}Cr_{30}$	BCC	0.591	5.00	3.100	6.534	51.38	[41]
3	$Ti_{25}V_{30}Nb_{10}Cr_{35}$	BCC	0.585	5.10	3.079	6.497	49.20	[41]
4	$Ti_{25}V_{30}Nb_{10}Cr_{33}Fe_2$	BCC	0.582	5.14	3.062	6.511	45.65	[42]
5	$Ti_{25}V_{30}Nb_{10}Cr_{31}Fe_4$	BCC	0.578	5.18	3.054	6.525	44.73	[42]
6	$Ti_{25}V_{30}Nb_{10}Cr_{33}Mo_2$	BCC	0.575	5.10	3.085	6.417	44.65	[43]
7	$Ti_{25}V_{30}Nb_{10}Cr_{31}Mo_4$	BCC	0.565	5.10	3.090	6.331	43.39	[43]
8	$Ti_{25}V_{30}Nb_{10}Cr_{29}Mo_6$	BCC	0.555	5.10	3.097	6.240	41.82	[43]
9	$Ti_{40}Cr_{45}Mo_{10}Mn_5$	BCC	0.544	5.25	3.088	7.260	34.50	[22]
10	$Ti_{40}Cr_{50}Mo_{10}$	BCC	0.538	5.20	3.082	7.480	33.75	[44]
11	$Ti_{40}Cr_{49}Mo_{10}Fe_1$	BCC	0.536	5.22	3.075	7.481	34.50	[44]
12	$Ti_{40}Cr_{48}Mo_{10}Fe_2$	BCC	0.535	5.24	3.058	7.487	32.40	[44]
13	$Ti_{35}Cr_{50}Mo_{10}Nb_5$	BCC	0.535	5.25	3.078	7.360	31.76	[22]
14	$Ti_{40}Cr_{47}Mo_{10}Fe_3$	BCC	0.533	5.26	3.040	7.494	30.40	[44]

BCC: Body-centered cubic; EDV_{alloy}: electronegativity difference value of the alloy; ΔH_{des}: desorption enthalpy.

In contrast, as shown in Figure 1E, ΔH_{des} increases almost monotonically with EDV_{alloy} and exhibits a higher correlation with the fitting than with the lattice constant, δ, and VEC. This quantitative comparison further indicates that EDV_{alloy} is more effective than the other descriptors in explaining alloys with similar VEC values but different hydride stability. The underlying physical mechanism can be explained in terms of charge transfer and M-H bonding: during hydrogen absorption and desorption, hydrogen interacts electronically with surrounding metal atoms, leading to partial charge transfer from the metal to hydrogen and the formation of M-H bonds that exhibit both ionic and covalent character. The greater the EDV_{alloy}, the stronger the driving force for electron transfer from the metal to hydrogen, the stronger the average M-H interaction, and the more stable the hydride; conversely, a smaller EDV_{alloy} indicates that the alloy's average electronegativity is closer to that of hydrogen, weakening the driving force for electron transfer from the metal to hydrogen and reducing the average M-H bond strength, thereby promoting hydride destabilization[21,38,39]. Furthermore, hydrogen has an electronegativity of 2.2, while transition metals generally have electronegativities lower than 2.2; even among elements with the same *VEC* (such as V and Nb, both with *VEC* = 5), there are subtle differences in electronegativity[40]. Therefore, EDV_{alloy} can serve as an effective empirical parameter for describing the thermodynamic trends in hydrogen release in BCC hydrogen-storage HEAs. The phase structures, key parameters, and ΔH_{des} values of the 14 compiled alloys are summarized in Table 1.

Based on the above analysis, thermodynamic control of BCC hydrogen storage HEAs in the TiVZrNb system was further conducted using EDV_{alloy} composition design parameters. The design objective was to moderately reduce the stability of alloy hydrides while maintaining a single-phase BCC structure and high hydrogen storage capacity, thereby improving hydrogen release performance. In the TiVZrNb quaternary system, the Pauling electronegativities of the elements are, in order: Zr = 1.33, Ti = 1.54, Nb = 1.60, and V = 1.63, all of which are lower than the electronegativity of H (2.20). Among these elements, Zr and Ti have relatively lower electronegativities and therefore contribute to a larger average electronegativity difference between the alloy and H. In contrast, Nb and V have relatively higher electronegativities, and increasing the Nb content raises the alloy's average electronegativity and reduces EDV_{alloy} [Figure 1F]. Therefore, this study employs a method

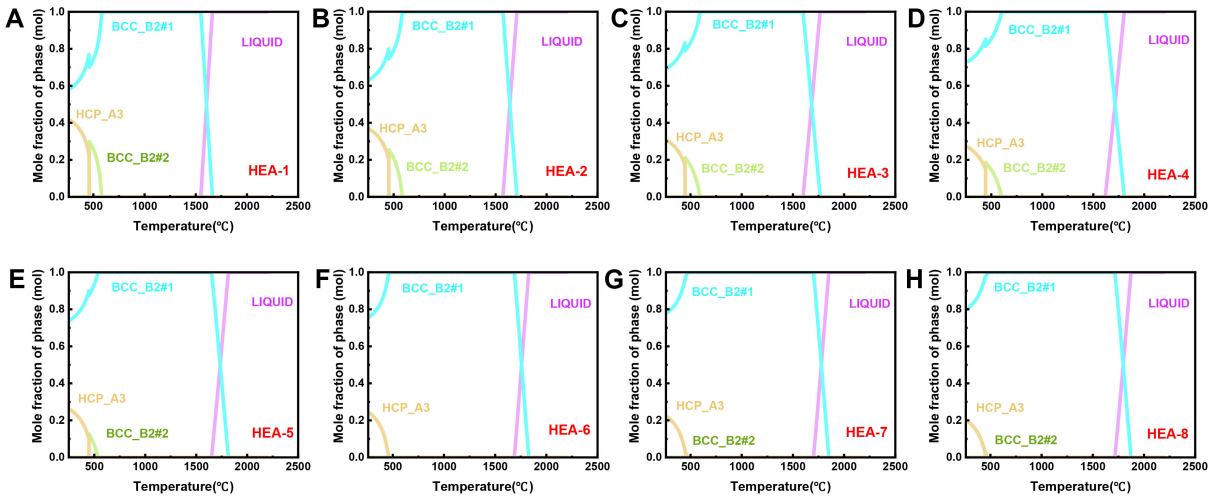

Figure 2. Phase diagrams for HEA-1 to HEA-8 alloys calculated using Thermo-Calc software: (A) HEA-1, (B) HEA-2, (C) HEA-3, (D) HEA-4, (E) HEA-5, (F) HEA-6, (G) HEA-7, and (H) HEA-8. BCC_B2#1 and BCC_B2#2 denote two distinct composition sets of the BCC/B2 thermodynamic phase model generated by Thermo-Calc; HCP_A3 denotes the hexagonal close-packed solid-solution phase; and LIQUID denotes the liquid phase. BCC: Body-centered cubic; HCP: hexagonal close-packed; HEA: high-entropy alloy.

Table 2. Atomic ratios, EDV_{alloy}, VEC, and δ for alloys HEA-1 to HEA-8

Alloy	Composition	EDV_{alloy}	VEC	δ (%)
HEA-1	$Ti_{40}V_{30}Zr_{10}Nb_{20}$	0.6420	4.5	5.99
HEA-2	$Ti_{35}V_{30}Zr_{10}Nb_{25}$	0.6390	4.55	5.97
HEA-3	$Ti_{30}V_{30}Zr_{10}Nb_{30}$	0.6360	4.6	5.94
HEA-4	$Ti_{25}V_{30}Zr_{10}Nb_{35}$	0.6330	4.65	5.92
HEA-5	$Ti_{27.5}V_{30}Zr_{7.5}Nb_{35}$	0.6278	4.65	5.59
HEA-6	$Ti_{30}V_{30}Zr_{5}Nb_{35}$	0.6225	4.65	5.22
HEA-7	$Ti_{27.5}V_{30}Zr_{5}Nb_{37.5}$	0.6210	4.675	5.19
HEA-8	$Ti_{25}V_{30}Zr_{5}Nb_{40}$	0.6195	4.70	5.17

VEC: Valence electron concentration; EDV_{alloy}: electronegativity difference value of the alloy; HEA: high-entropy alloy; δ: lattice distortion.

to reduce the Ti/Zr content and increase the Nb content, thereby continuously regulating the EDV_{alloy} composition. Concurrently, the V content was fixed at 30 at. % in all alloys to minimize the impact of V content variations on the stability of the BCC phase and hydrogen storage capacity. The specific compositions and key parameters are shown in Table 2. As the Ti and Zr contents decrease, the alloy's electronegativity difference gradually decreases; it is anticipated that the stability of the alloy hydrides will consequently weaken, thereby improving hydrogen desorption performance. Since the second phase significantly affects the hydrogen storage plateau and thermodynamic parameters - for example, the C14 Laves phase, Zr-rich phase, or other intermetallic compounds may introduce additional hydrogen absorption and desorption reaction processes - this study first requires the designed alloys to possess a stable single-phase BCC region during the composition design stage. To this end, the TCHEA6 database in Thermo-Calc software was used to predict the equilibrium phase compositions of HEA-1 to HEA-8. The calculation results are shown in Figure 2, indicating that all alloys exhibit a wide single-phase BCC temperature range near 1,473 K. Therefore, in this study, the as-cast alloys were subjected to homogenization annealing at 1,473 K followed by water quenching to obtain a single-phase BCC solid solution with uniform composition, thereby eliminating the interference of the second phase on the subsequent thermodynamic analysis of hydrogen release and further verifying the regulatory effect of EDV_{alloy} on the thermodynamics of hydrogen release in TiVZrNb BCC hydrogen-storage HEAs.

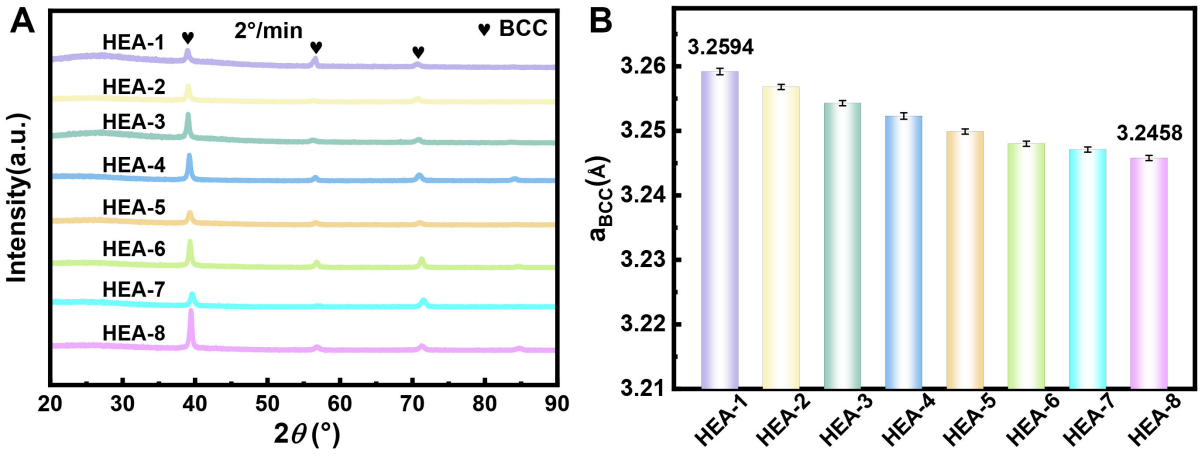

Figure 3. (A) XRD patterns of HEA-1 to HEA-8 collected at a scan rate of 2°/min; (B) corresponding lattice parameters obtained by GSAS-II refinement. Error bars in (B) represent the standard uncertainties obtained from GSAS-II refinement. BCC: Body-centered cubic; HEA: high-entropy alloy; XRD: X-ray diffraction; GSAS-II: General Structure Analysis System II.

Phase structure and microstructure

Figure 3 and Supplementary Figures 1 and 2 show the X-ray diffraction (XRD) spectrum of alloys HEA-1 to HEA-8. As shown in the Figure 3A, all alloys exhibit only characteristic diffraction peaks of the BCC structure. The peaks at approximately 2θ = 40°, 56°, and 71° correspond to the (110), (200), and (211) crystal planes of the BCC structure, respectively; no diffraction peaks from a second phase were observed. The lattice parameters of the alloys were refined using the Rietveld method with GSAS-II software, and the results are listed in Supplementary Table 2. As the Nb content increased, and the Zr and Ti contents decreased, the lattice parameter a of the alloy decreased from 3.2594 Å to 3.2458 Å. This is because Nb partially substitutes for Zr and Ti, and the atomic radius of Nb (1.429 Å) is smaller than that of Zr (1.603 Å) and Ti (1.462 Å), resulting in a decrease in the average atomic radius of the alloy and a more compact lattice packing, thereby reducing the lattice parameters.

To further characterize the microstructure of the alloys, BSE and energy-dispersive X-ray spectroscopy (EDS) analyses were performed on the heat-treated alloys; the results are shown in Figure 4. The microstructure of all alloys (HEA-1 to HEA-8) exhibited an approximately equiaxed grain structure. Due to differences in crystal orientation between grains, distinct contrast differences were observed in the backscattered electron images, allowing for clear identification of grain boundaries. No second phase was detected, further confirming that the alloys have a single-phase BCC structure, consistent with the XRD results. The corresponding EDS results [Figure 4A'-H'] show that various elements are uniformly distributed within the alloys, with no regional compositional segregation observed. Furthermore, the alloy compositions determined by EDS are nearly consistent with the designed nominal values. Higher-magnification BSE images and the corresponding EDS elemental maps of HEA-1 to HEA-8 are shown in Supplementary Figure 3, and EDS line-scan results of the representative HEA-8 alloy across the grain boundary and grain interior regions are shown in Supplementary Figure 4. These results show no obvious secondary phase contrast or elemental enrichment/depletion at the SEM-EDS detection scale, further supporting the chemical homogeneity of the alloys.

Hydrogen absorption kinetics

To investigate the alloy's hydrogen storage capacity, hydrogen absorption kinetics tests were conducted on heat-treated samples. Figure 5 shows the hydrogen absorption kinetics curves for the activated samples at 303 K and 5 MPa hydrogen pressure. As shown in the figure, all samples exhibited rapid hydrogen absorption

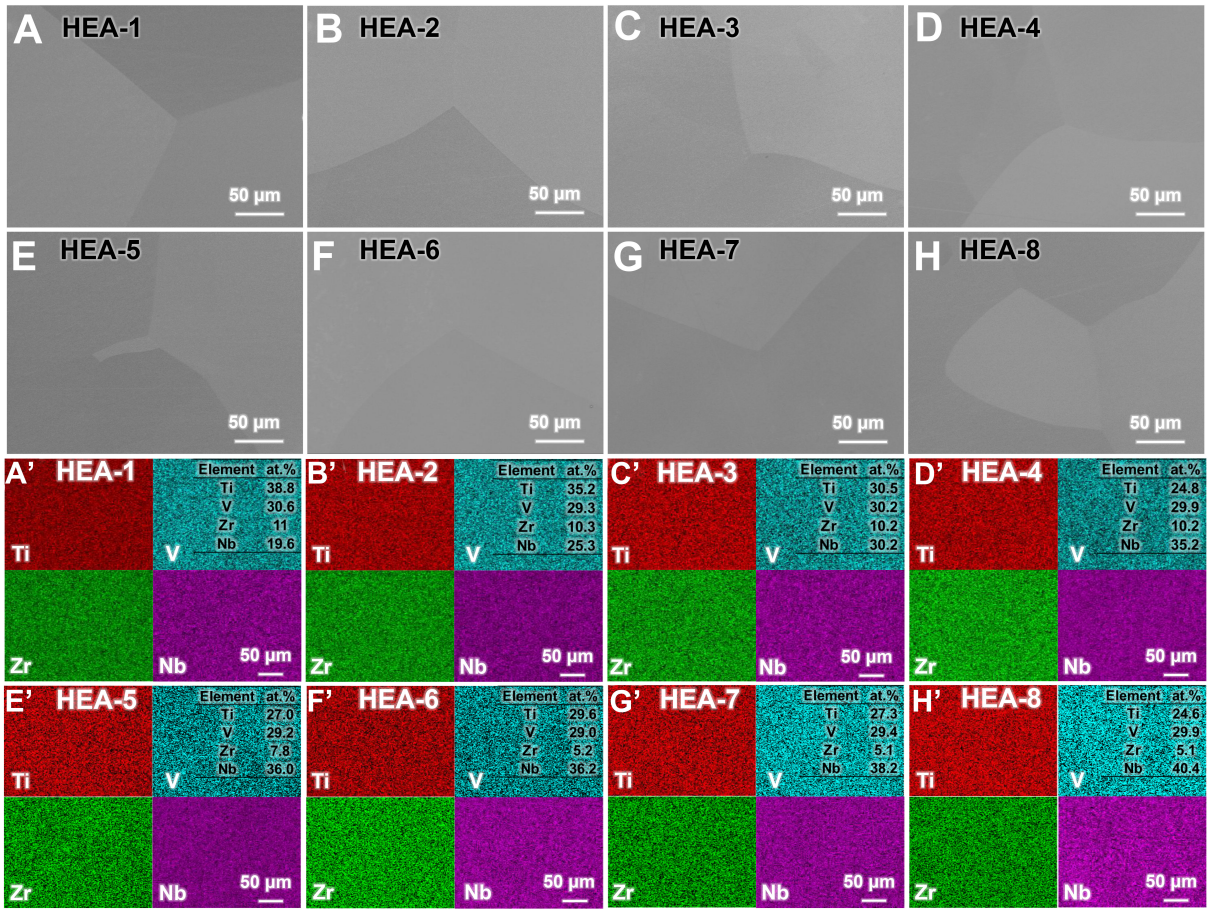

Figure 4. The BSE images (A-H) and the corresponding EDS maps (A'-H') of HEA-1 to HEA-8 alloys. HEA: High-entropy alloy; BSE: backscattered electron; EDS: energy-dispersive X-ray spectroscopy.

kinetics, reaching their saturated hydrogen storage capacity within 150 s. Among them, HEA-8 demonstrated the most outstanding hydrogen absorption kinetics, reaching its saturated hydrogen storage capacity in just 75 s. It is worth noting that no significant correlation was observed between hydrogen absorption kinetics and the electronegativity difference, indicating that, within the composition range studied, reducing the EDV_{alloy} did not have a significant adverse effect on the alloy's rapid hydrogen absorption behavior. Although some fluctuations were observed among the intermediate alloys, the gravimetric hydrogen storage capacity showed an overall decreasing trend from 3.12 wt.% for HEA-1 to 2.86 wt.% for HEA-8 as EDV_{alloy} decreased. This trend is primarily attributed to differences in the relative atomic masses of the elements. When the mass hydrogen storage capacity is converted to the hydrogen-to-metal atomic ratio (H/M), the H/M values for HEA-1 to HEA-8 were 2.00, 2.01, 2.01, 2.01, 2.02, 2.01, 2.02, and 2.02, respectively. The repeated initial hydrogen absorption measurements used to calculate the standard deviations of the H/M values in Figure 5B are shown in Supplementary Figure 5. These values are significantly higher than the H/M value (1.75) reported by Montero *et al.*[16] for the $Ti_{0.325}V_{0.275}Zr_{0.125}Nb_{0.275}$ alloy, reaching the theoretical maximum H/M value for high-entropy alloys with a BCC structure, indicating that the optimized alloys in this series possess excellent hydrogen storage capacity.

Hydrogen storage thermodynamics

To further investigate the thermodynamic properties of the alloy, PCT curves were measured at various temperatures [Figure 6] to verify whether EDV_{alloy} can effectively regulate hydride stability. Detailed thermodynamic parameters for hydrogen absorption and desorption are summarized in Supplementary Table 3. The PCT curves reveal that the thermodynamic behavior of the TiVZrNb alloy system is consistent

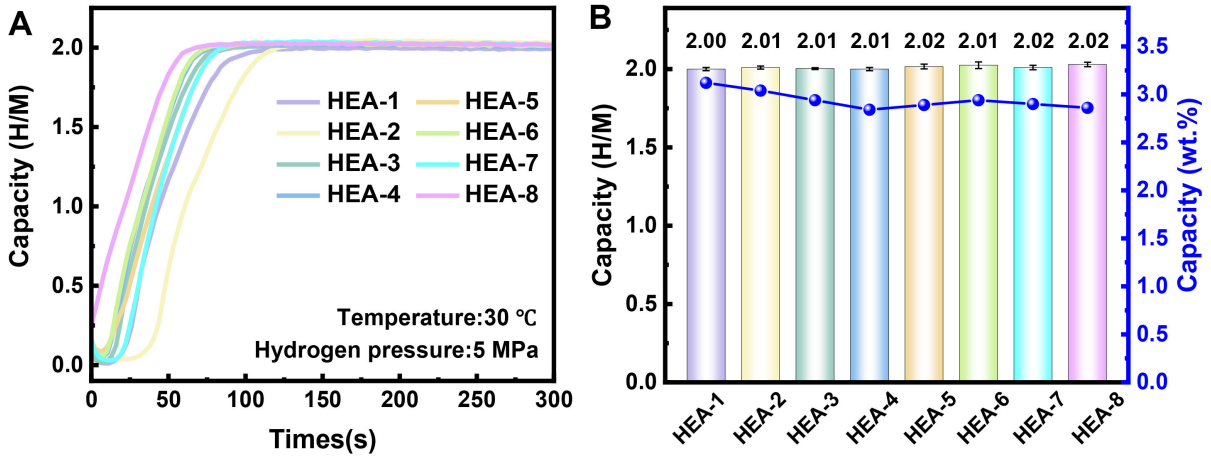

Figure 5. (A) Initial hydrogen absorption kinetics curves for activated alloys HEA-1 to HEA-8 at 303 K and 5 MPa hydrogen pressure, along with (B) their mass hydrogen storage capacity and H/M values. Error bars in (B) represent the standard deviations obtained from repeated Sievert measurements (n = 3 for HEA-1-HEA-5 and n = 2 for HEA-6-HEA-8). HEA: High-entropy alloy; H/M: hydrogen-to-metal atom ratio.

with that of typical BCC hydrogen storage alloys, specifically exhibiting two plateau regions, indicating the presence of two hydrogen-induced phase transformations[11]. During the initial hydrogen absorption stage, hydrogen exists in the alloy's interstitial sites in the form of a solid solution (α phase). When the hydrogen concentration reaches the alloy's solubility limit, a hydrogen-induced phase transformation occurs, forming the β_1 phase; at this point, the alloy enters the first plateau region (where the α phase and β_1 phase coexist). Since the plateau pressure in this region is extremely low, exceeding the detection range of the instrument's pressure accuracy, its plateau characteristics are not observed in Figure 6. As the hydrogen absorption process continues, the β_1 phase gradually transforms into the β_2 phase. Once the β_1 phase has completely converted to the β_2 phase, a further increase in hydrogen concentration initiates the formation of the γ phase, at which point the alloy enters the second plateau region (where the β_2 and γ phases coexist)[45]. This plateau primarily reflects the alloy's thermodynamic properties. It can also be observed that as the temperature rises, the alloy's plateau pressure increases accordingly. This is because the hydrogen absorption process is exothermic, while the hydrogen desorption process is endothermic. The hydrogen absorption and desorption reactions are reversible; increasing temperature favors hydrogen desorption but hinders absorption. Therefore, for hydrogen absorption, a higher hydrogen pressure is required to drive the reaction forward, resulting in a higher plateau pressure. For hydrogen desorption, high temperatures are favorable, promoting hydride decomposition and hydrogen release[22,46]. Meanwhile, the absorption and desorption plateau pressures are clearly separated, indicating pronounced absorption-desorption hysteresis in this alloy series. This hysteresis is mainly associated with the β monohydride-γ dihydride transformation, which involves the structural transition between the BCC-type monohydride-related state and the hydrogen-rich face-centered cubic (FCC) dihydride state. During forward and reverse transformations, lattice expansion/contraction, lattice mismatch, elastic strain, interfacial energy, and distinct nucleation/interface migration barriers can lead to distinct driving forces for hydrogen absorption and desorption, resulting in separate absorption and desorption plateau pressures[47,48]. In addition, local lattice distortion and heterogeneous hydrogen site energies in the TiVZrNb solid solution may also contribute to plateau slope and hysteresis[49]. Additionally, the PCT curves show that the maximum hydrogen storage capacity (H/M) for all alloys is 2, consistent with the results of kinetic tests.

Due to significant differences in the thermodynamic parameters across all alloys, it is difficult to directly compare their pressure parameters at a given temperature. To more reasonably compare the relative stability

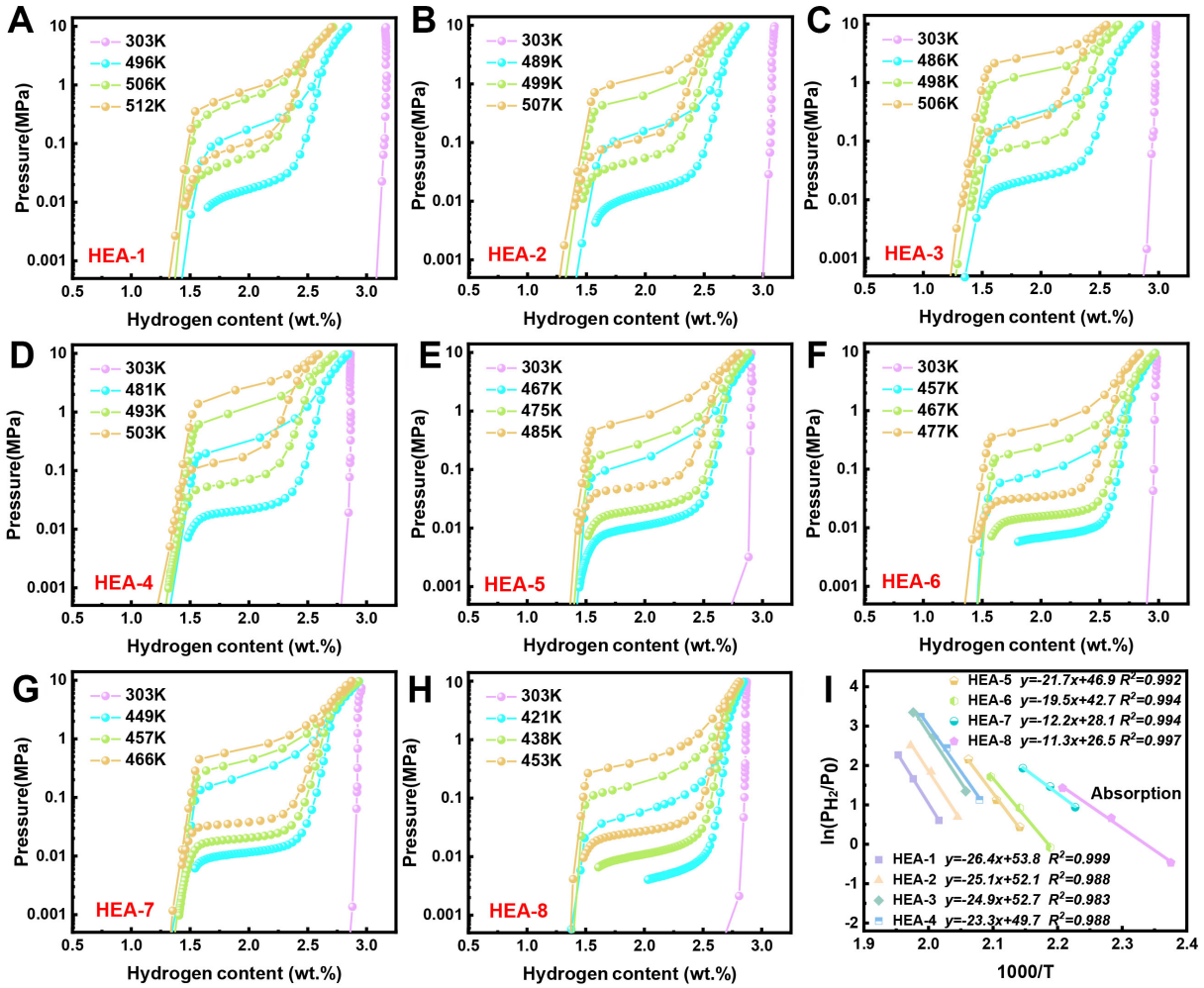

Figure 6. Complete hydrogen absorption-desorption PCT curves of (A) HEA-1, (B) HEA-2, (C) HEA-3, (D) HEA-4, (E) HEA-5, (F) HEA-6, (G) HEA-7, and (H) HEA-8 at different temperatures, together with (I) the Van't Hoff fitting results obtained from the hydrogen absorption plateau pressures. HEA: High-entropy alloy; PCT: pressure-composition isotherm.

of alloy hydrides, the enthalpy change (ΔH) and entropy change (ΔS) during the hydrogen absorption/desorption reactions were calculated using the Van't Hoff equation (Equation 1). The actual PCT temperatures used for the Van't Hoff analysis are listed in Supplementary Table 3 for each alloy. The 303 K curves shown in Figure 6 were used to illustrate the initial hydrogen absorption behavior and were not included in the Van't Hoff fitting. Only the plateau pressures measured at the temperatures listed in Table S3 were used for the thermodynamic analysis. It should be noted that the first extremely low-pressure plateau observed in the PCT curves is associated with the formation/decomposition of a highly stable β-hydride phase. Because the equilibrium pressure of this β-hydride plateau is very low and close to or beyond the reliable pressure range of the Sieverts-type apparatus, it was not used for the Van't Hoff fitting. In contrast, the plateau pressures listed in Supplementary Table 3 correspond to the subsequent main measurable plateau, which is related to the practical reversible hydrogen storage capacity of the alloys. Therefore, excluding the first extremely low-pressure plateau does not affect the thermodynamic analysis of the main reversible absorption/desorption process. The obtained ΔH_{abs} and ΔH_{des} values should be regarded as apparent thermodynamic parameters of the main reversible plateau rather than those of the highly stable β-hydride plateau. Figures 6I and 7A show the Van't Hoff fitting results for the hydrogen absorption and desorption processes, respectively. The entropy and enthalpy changes for the hydrogen absorption and desorption reactions were obtained from the slopes and intercepts of the linear fits [Supplementary Table 3].

Figure 7B further illustrates the relationship between the ΔH_{des} values of the HEA-1 to HEA-8 alloys and EDV_{alloy}. As EDV_{alloy} decreases from 0.6420 to 0.6195, ΔH_{des} decreases from 230.3 kJ/mol H_2 to 97.3 kJ/mol H_2, demonstrating a clear positive correlation between the two. Figure 7C summarizes the corresponding enthalpy changes for hydrogen absorption and desorption. This trend indicates that as the alloy composition is adjusted, hydride stability gradually decreases, the heat required for hydride decomposition decreases, and hydrogen desorption becomes increasingly thermodynamically favorable. This result is consistent with the earlier composition design prediction based on the electronegativity difference: reducing the average electronegativity difference between the alloy and H weakens the average M-H interaction, thereby reducing the thermodynamic stability of the hydride. From a compositional perspective, the Ti/Zr content gradually decreases from HEA-1 to HEA-8, while the Nb content gradually increases. Since Nb has a higher Pauling electronegativity than Ti and Zr, increasing the Nb content raises the alloy's average electronegativity, thereby reducing the average electronegativity difference between the alloy and H. A smaller EDV_{alloy} value indicates a weakened driving force for average charge transfer from the metal to hydrogen and reduced M-H bond strength; consequently, the hydrogen-rich hydride phase decomposes more readily, as evidenced by a lower ΔH_{des}. To further compare the influence of different descriptors within the designed HEA-1 to HEA-8 series, the correlations between ΔH_{des} and EDV_{alloy}, VEC, lattice constant, and δ were analyzed by linear fitting, as shown in Figure 8. The corresponding R^2 and p values were added to each panel to provide a quantitative comparison rather. Compared to VEC, lattice constant, and δ, EDV_{alloy} exhibits a clearer positive correlation with ΔH_{des}. This indicates that the alloy-hydrogen average electronegativity difference can effectively reflect the trend in the average M-H interaction strength in single-phase BCC alloys and serves as an effective empirical parameter for guiding the thermodynamic regulation of hydrogen release in BCC high-entropy hydrogen storage alloys. However, it must be noted that hydride stability is not determined solely by the EDV_{alloy} factor. In the HEA-1 to HEA-8 series, EDV_{alloy} changes together with VEC, δ, lattice parameter, Ti/Zr content, and Nb content, indicating that the effect of EDV_{alloy} is inevitably coupled with compositional and structural factors. In particular, the alloy's lattice parameters can influence $\Delta Hdes$ by affecting the interstitial space available for hydrogen occupation, the stability of hydrogen in interstitial sites, and the repulsive interactions between neighboring hydrogen atoms. In both the statistical data and the experimental results for HEA-1 to HEA-8 in this study, ΔH_{des} shows the strongest monotonic correlation with EDV_{alloy}. Meanwhile, the strong correlation between lattice constant and ΔH_{des} in Figure 8 also indicates that the lattice-size effect cannot be ignored in this composition series. Therefore, EDV_{alloy} is more suitable as a first-order empirical descriptor in composition design than as the sole parameter to completely replace structural and electronic factors. A more rigorous distinction between the contributions of EDV_{alloy} and lattice-related factors requires the design of control alloy series with decoupled electronegativity and lattice-size parameters. This will be an important direction for future work to further clarify the relative contribution of EDV_{alloy} to hydride stability.

Analysis of alloy dehydrogenation behavior

To further verify the influence of EDV_{alloy} on actual dehydrogenation behavior, TDS curves for alloys HEA-1 through HEA-8 were measured at a heating rate of 5 K/min [Figure 9], and all results were subjected to Gaussian peak deconvolution analysis. The results show that the TDS curves of all alloys can be decomposed into three hydrogen desorption peaks: a low-temperature peak (Peak 1) and high-temperature peaks (Peak 2 and Peak 3). This indicates that HEA-1 to HEA-8 exhibit similar multi-stage dehydrogenation processes, corresponding to the gradual decomposition of different hydride phases or distinct hydrogen-occupation states following hydrogen absorption.

It should be noted that the three-peak deconvolution was applied to the entire HEA-1 to HEA-8 alloy series, rather than being established solely from the hydrogen-content-dependent analysis of HEA-8. Since these alloys share the same constituent elements and differ primarily in their relative compositions, their principal

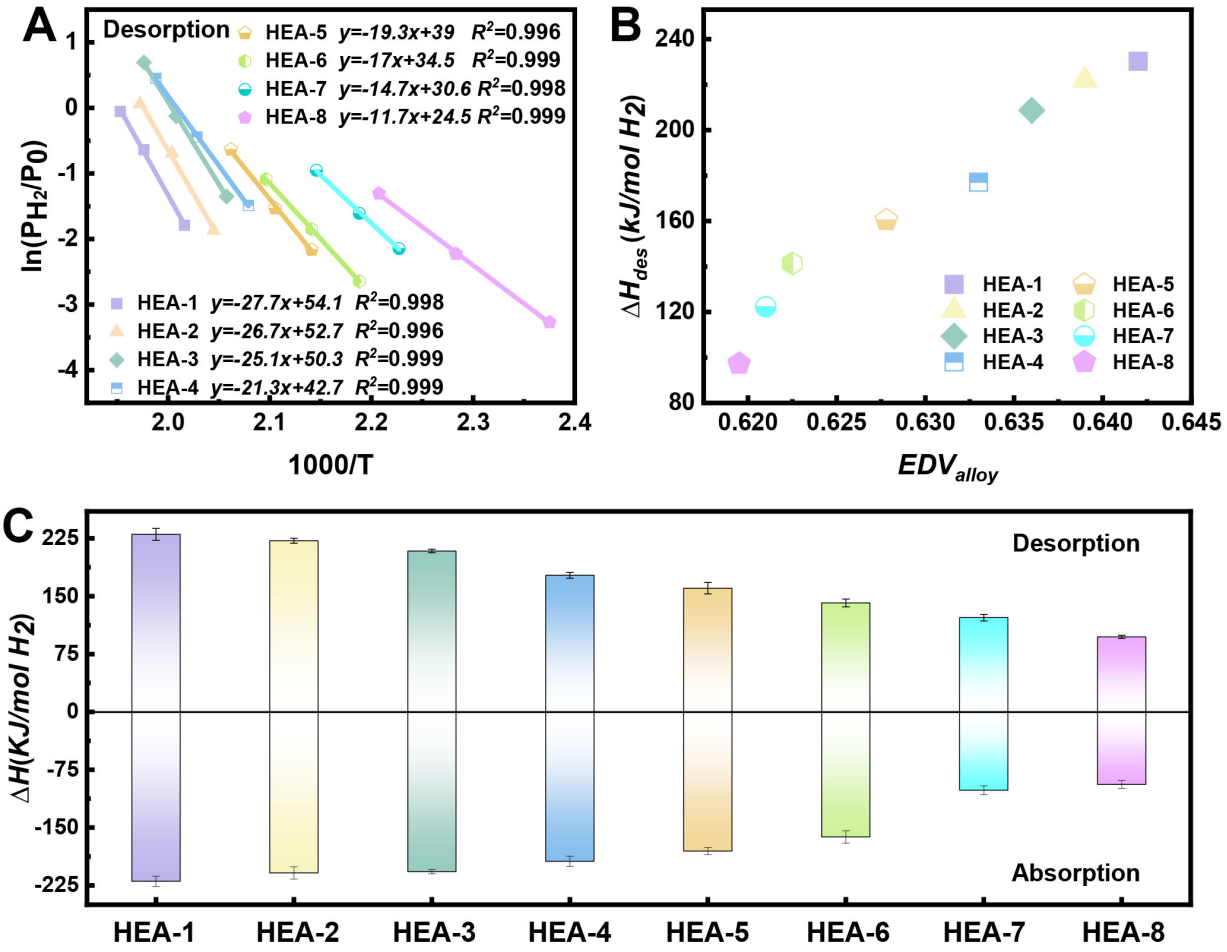

Figure 7. Van't Hoff fitting of the hydrogen desorption process (A), the correlation between ΔH_{des} and EDV_{alloy} (B), and the corresponding enthalpy changes for hydrogen absorption and desorption (C) for alloys HEA-1 to HEA-8. Error bars represent the uncertainties calculated from the standard errors of the Van't Hoff linear fittings. EDV_{alloy}: Electronegativity difference value of the alloy; HEA: high-entropy alloy; ΔH_{des}: desorption enthalpy.

hydrogen-induced phase transformations and dehydrogenation processes are expected to be similar, whereas hydride stability varies systematically with composition. The small sharp features observed near the low-temperature peak in HEA-5 to HEA-8 were not treated as independent desorption peaks. Since the TDS signal reflects the hydrogen release rate, these features may be related to transient fluctuations in the desorption rate caused by reduced hydride stability and accelerated low-temperature dehydrogenation. Therefore, the deconvolution focuses on the main desorption contributions rather than on every minor local fluctuation. As EDV_{alloy} decreases, the peak temperature of Peak 1 gradually decreases from 632 K in HEA-1 to 509 K in HEA-8, and the peak temperature of Peak 2 decreases from 681 K (HEA-1) to 533 K (HEA-8). This indicates that reducing EDV_{alloy} can significantly lower the dehydrogenation temperature of the main hydride phase, consistent with the observed reduction in ΔH_{des} in the Van't Hoff analysis. In other words, as the average electronegativity difference between the alloy and H decreases, the average M-H interaction weakens, making the hydride more prone to decomposition during heating. In contrast, the peak temperature of Peak 3 shows little change from HEA-3 to HEA-8, indicating that the hydrogen release process corresponding to this peak is relatively insensitive to EDV_{alloy}.

To further clarify the structural transformation processes corresponding to each dehydrogenation peak in the TDS, HEA-8 - which exhibits the lowest thermodynamic stability for hydrogen release and the lowest dehydrogenation peak temperature - was selected as the representative sample for stepwise dehydrogenation

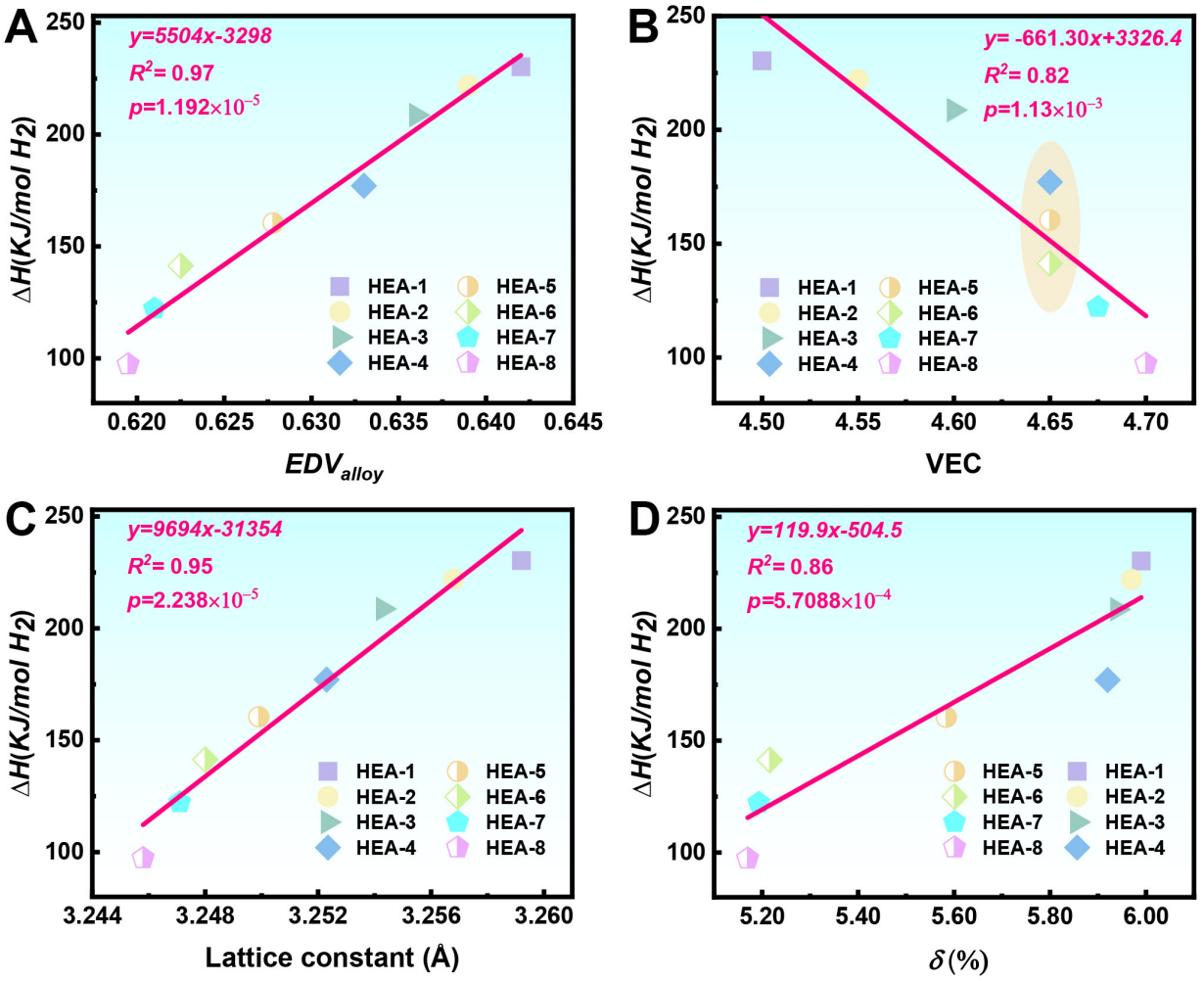

Figure 8. Correlation between the ΔH_{des} in HEA-1 to HEA-8 alloys, and their EDV_{alloy} (A), *VEC* (B), lattice constants (C), and δ (D). The linear fitting results, including R^2 and *P-values,* are shown in the corresponding panels. HEA: High-entropy alloy; ΔH_{des}: desorption enthalpy; EDV_{alloy}: electronegativity difference value of the alloy; VEC: valence electron concentration; δ: lattice distortion.

analysis. Figure 10A shows the PCT curve of HEA-8 at 453 K. By controlling the cutoff hydrogen pressure during PCT testing, samples with hydrogen contents of 2.83, 1.88, 1.32, and 1.18 wt.% were obtained. TDS measurements determined the actual hydrogen content of the samples at each stage [Supplementary Figure 6], with the vertical axis representing the hydrogen release rate (ppm/s) and the horizontal axis representing time. By integrating over time, the actual hydrogen contents of the samples at each stage were determined to be 28,340, 18,840, 13,230, and 11,750 ppm (weight ppm, unless otherwise mentioned), with corresponding H/M atomic ratios of 2.00, 1.31, 0.92, and 0.81. At a heating rate of 5 K/min, TDS testing and Gaussian peak deconvolution were performed on samples with varying hydrogen content, and the results are shown in Figure 10B. The TDS curve of the $MH_{2.00}$ sample can be decomposed into three hydrogen release peaks with peak temperatures of 509, 533, and 723 K; the $MH_{1.31}$ sample also exhibits three hydrogen release peaks with peak temperatures of 551, 570, and 721 K; the $MH_{0.92}$ sample decomposed into two hydrogen release peaks with peak temperatures of 586 and 725 K; the $MH_{0.81}$ sample also exhibited two hydrogen release peaks with peak temperatures of 598 and 723 K. It can be seen that as the hydrogen content decreases, the peak hydrogen release rates gradually decrease. The areas of the hydrogen release peaks correspondingly shrink.

To further establish the correlation between the dehydrogenation peak and structural transitions, XRD measurements at a scan rate of 2°/min were performed on samples with different hydrogen contents, and the results are shown in Figure 10C. The diffraction pattern of the $MH_{2.00}$ sample exhibits a single FCC structure

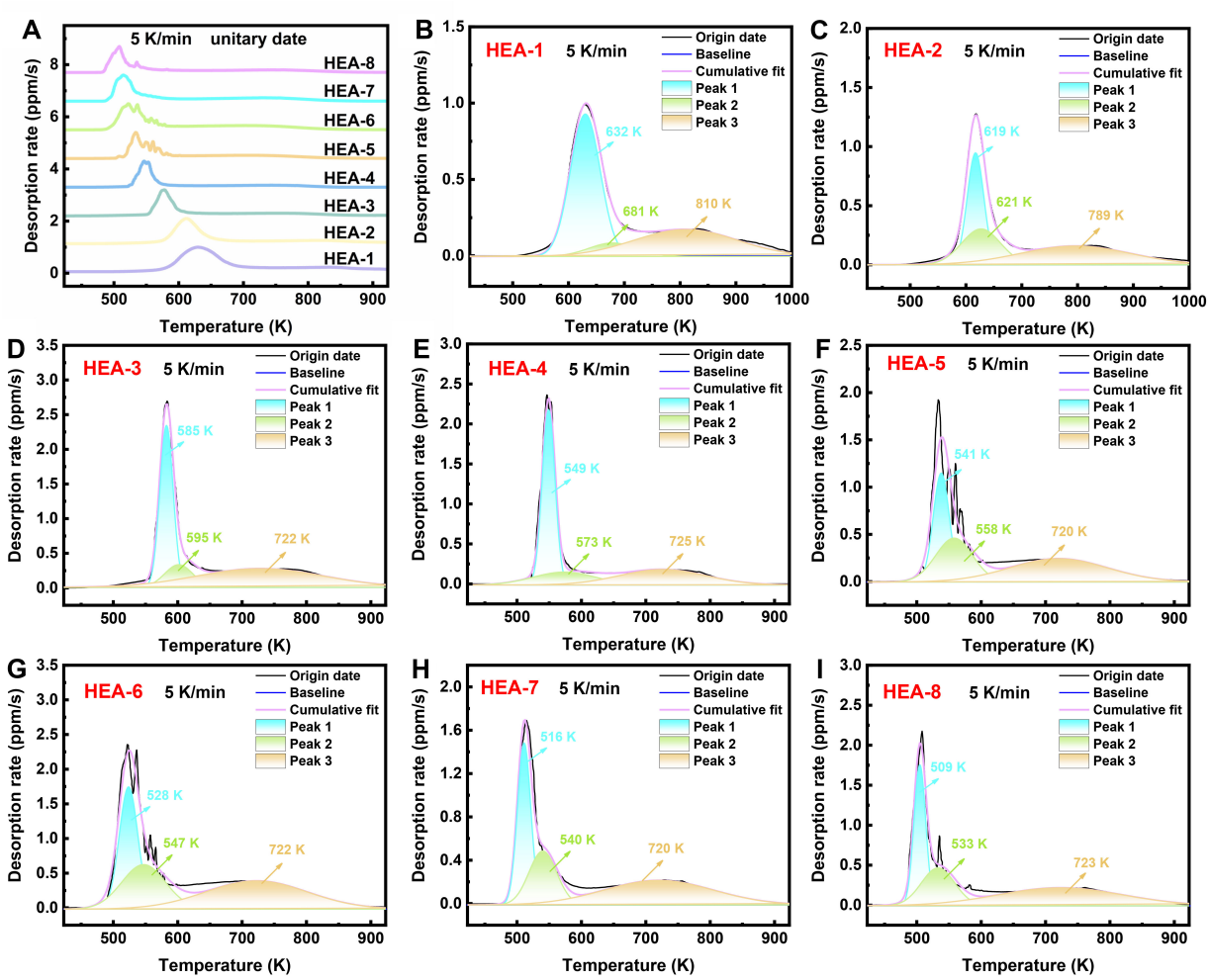

Figure 9. TDS of alloys HEA-1 to HEA-8 at a heating rate of 5 K/min: (A) comparison of TDS curves for different alloys; (B-I) peak fitting analysis of hydrogen desorption peaks. The curves in (A) are vertically offset for clarity. HEA: High-entropy alloy; TDS: thermal desorption spectroscopy.

with a lattice constant a = 4.464 Å, indicating that the sample is a dihydride (γ phase), consistent with previous reports[50]. Upon dehydrogenation to $MH_{1.31}$, the sample exhibited coexistence of FCC and BCC phases, with the BCC phase having a lattice constant of 3.388 Å and the FCC phase's lattice constant decreasing slightly to 4.461 Å. For BCC-based hydrogen storage alloys, the stability of the dihydride (FCC) is typically much lower than that of the monohydride (BCC); therefore, Peak 1 can be attributed to the dehydrogenation peak of the dihydride to the monohydride. Upon further hydrogen release to $MH_{0.92}$, the sample's FCC diffraction peak completely disappeared, transforming into a single BCC structure corresponding to the monohydride phase (*β* phase), with a lattice constant of a = 3.368 Å. At this point, Peak 1 completely disappeared, further confirming that it corresponds to the dehydrogenation of the dihydride. When hydrogen was released to $MH_{0.81}$, the sample retained a single BCC structure, but the lattice constant decreased from 3.368 Å to 3.357 Å, due to lattice contraction caused by hydrogen release. By subjecting the sample to dynamic vacuum pumping at 773 K, a fully dehydrogenated sample can be obtained [Supplementary Figure 7], which reversibly recovers to the initial BCC structure, with a lattice constant similar to that of the original, hydrogen-unabsorbed sample. Based on the above results, Peak 2 is primarily attributed to hydrogen desorption from the monohydride (*β* phase). In contrast, Peak 3 may be associated with the further release of more stable residual hydrogen from the *β* phase and/or the BCC solid-solution *α* phase. Combining the above analyses, the hydrogen release pathway of the HEA-8 alloy can be qualitatively

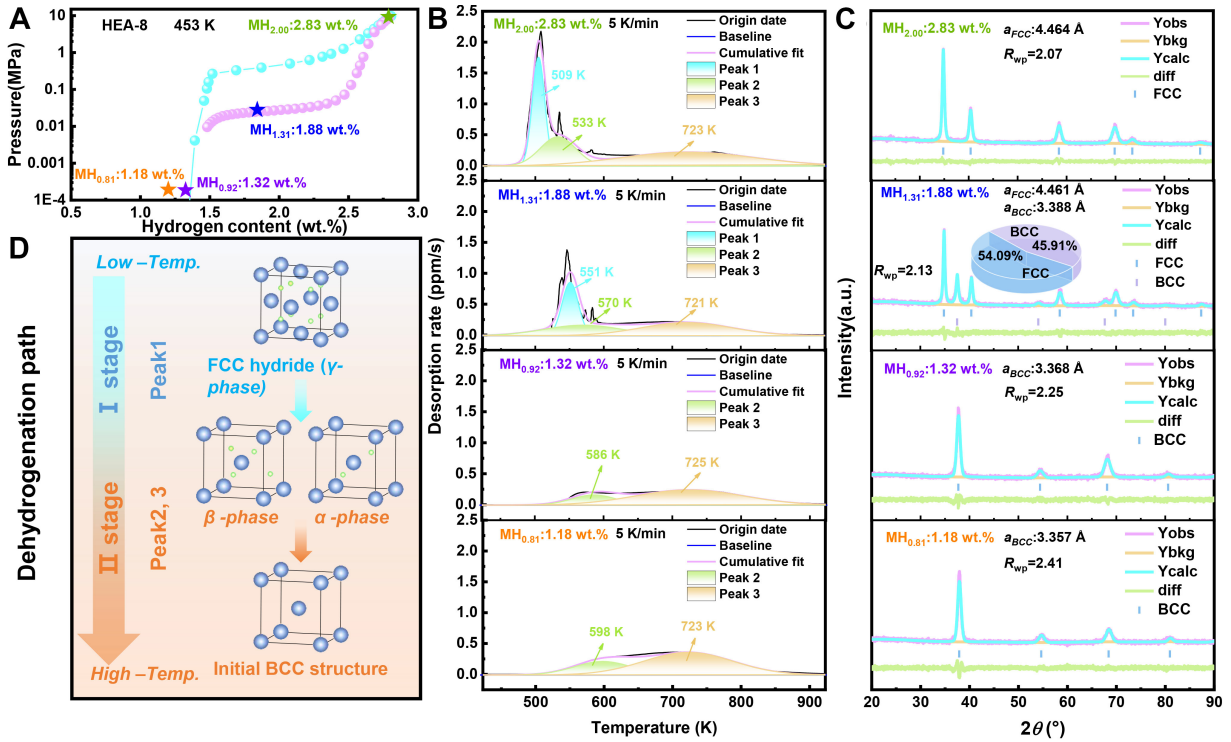

Figure 10. Analysis of the hydrogen absorption and desorption behavior of the HEA-8 alloy: (A) PCT curve at 453 K, (B) TDS spectra at different hydrogen contents, (C) corresponding XRD patterns, and (D) proposed hydrogen desorption processes corresponding to the different fitted peaks. HEA: High-entropy alloy; FCC: BCC: body-centered cubic; PCT: pressure-composition isotherm; TDS: thermal desorption spectroscopy; XRD: X-ray diffraction.

described as shown in Figure 10D: the low-temperature Peak 1 is mainly associated with the transformation of the FCC hydride (γ phase) to the BCC-type intermediate hydride (β phase), while the higher-temperature Peaks 2 and 3 are related to the further dehydrogenation of the β phase and/or BCC α phase[13]. This interpretation is consistent with the typical stepwise dehydrogenation behavior of BCC hydrogen storage alloys and related BCC high-entropy hydrides, in which the dehydrogenation process proceeds from a hydrogen-rich FCC dihydride to an intermediate monohydride and finally to a BCC structure. However, conventional *ex-situ* XRD cannot accurately quantify the hydrogen content or phase fraction in each phase, nor can it directly determine hydrogen occupation. Therefore, the present peak assignment should be regarded as a qualitative interpretation based on *ex-situ* XRD, TDS peak evolution, and reported *in-situ* results, rather than a definitive phase-resolved quantification. Further in situ XRD or neutron diffraction would be required to directly validate the high-temperature desorption contribution, especially for Peak 3.

Combining the changes in TDS peak temperatures for HEA-1 to HEA-8 reveals that the reduction in EDV_{alloy} primarily affects Peak 1 and Peak 2, corresponding to the stability of the hydrogen-rich FCC dihydride and BCC intermediate hydride phases. This indicates that reducing the average electronegativity difference between the alloy and hydrogen primarily weakens the average M-H interactions in high-hydrogen-content hydride phases, thereby increasing their susceptibility to dehydrogenation and decomposition. In contrast, the effect of EDV_{alloy} on Peak 3 is relatively weak. To further analyze the influence of EDV_{alloy} on the dehydrogenation process from a kinetic perspective, TDS curves for alloys HEA-1 to HEA-8 were measured at different heating rates, and the corresponding Gaussian deconvolution results are shown in Supplementary Figures 8-15, respectively. The apparent dehydrogenation activation energies were calculated using the Kissinger method, and the corresponding peak temperatures and activation energies are summarized in Supplementary Table 4. The Kissinger equation is as follows[44]:

$$\ln\left(\frac{\theta}{T_m^2}\right) = -\frac{E_a}{RT_m} + \ln(Y) \quad (5)$$

where T_m is the peak temperature, θ is the heating rate, E_a is the dehydrogenation activation energy, and R is the ideal gas constant. Figure 11 shows the TDS curves for HEA-1 to HEA-8 at different heating rates, along with the corresponding Kissinger fitting results. As the heating rate increases, Peak 1 consistently shifts toward higher temperatures for all alloys, while Peaks 2 and 3 generally exhibit an overall shift toward higher temperatures, with minor deviations for individual samples. This behavior is characteristic of a thermally activated dehydrogenation process. The Kissinger fitting results indicate that as the EDV_{alloy} decreases, the apparent dehydrogenation activation energy corresponding to Peak 1 gradually decreases. This suggests that the kinetic resistance to the transition from the FCC dihydride γ phase to the BCC intermediate hydride phase decreases, consistent with the aforementioned trend of decreasing Peak 1 temperature and ΔH_{des} in the PCT. Therefore, TDS and Kissinger analyses further support, from a kinetic perspective, the regulatory role of EDV_{alloy} on hydride stability. As EDV_{alloy} decreases, the average electronegativity difference between the alloy and hydrogen decreases, and the average M-H bond strength decreases, making the hydrogen-rich FCC dihydride phase more prone to decomposition, as evidenced by the decrease in the Peak 1 dehydrogenation peak temperature and the apparent dehydrogenation activation energy. Combined with the decrease in ΔH_{des} obtained from the PCT/Van't Hoff equation, this indicates that composition regulation based on EDV_{alloy} not only reduces the thermodynamic stability of the hydride but also lowers the kinetic resistance of the primary dehydrogenation process, thereby improving the hydrogen release performance of high-entropy BCC hydrogen storage alloys in the TiVZrNb system.

DISCUSSION

EDV_{alloy} as a thermodynamic descriptor for single-phase BCC hydrogen-storage HEAs

TiVZrNb-based BCC high-entropy hydrogen storage alloys possess high hydrogen storage capacity; however, the key issue limiting their practical application is their excessively high hydride stability. Therefore, it is crucial to reduce hydride stability while maintaining a single-phase BCC structure and a high H/M ratio. The results of this study indicate that, compared to VEC, lattice parameters, and δ, EDV_{alloy} shows a stronger correlation with ΔH_{des}. This suggests that EDV_{alloy} can more directly reflect the trend in hydride stability in single-phase BCC high-entropy hydrogen storage alloys. Furthermore, in the HEA-1 to HEA-8 series of alloys designed in this study, ΔH_{des} decreases correspondingly as EDV_{alloy} decreases. This result further validates the effectiveness of EDV_{alloy} as a thermodynamic control parameter: reducing the average electronegativity difference between the alloy and hydrogen can significantly lower the enthalpy of hydrogen desorption from hydrogen-rich hydrides, thereby thermodynamically destabilizing the hydrides. Existing first-principles calculations indicate that chemical contributions primarily govern changes in the dehydrogenation enthalpy of TiVZrNb-based hydrides; that is, the metal matrix's affinity for H is a key factor determining hydride stability, while structural and elastic contributions have a relatively minor impact on the differences in dehydrogenation enthalpy among various hydrides[39]. Therefore, the decrease in ΔH_{des} observed in this study, driven by the reduction in EDV_{alloy}, is likely primarily due to weakening of metal-hydrogen chemical interactions. From a bonding perspective, the electronegativity of Ti, V, Zr, and Nb is lower than that of H. After hydrogen absorption, H atoms enter the interstitial sites of the metal lattice and form a local M-H coordination environment with surrounding metal atoms. Existing first-principles studies of TiVZrNb-based hydrides further indicate that hybridization occurs between the H s state and the metal sp/d states, forming M-H bonding states. Meanwhile, Bader charge analysis reveals charge transfer from metal atoms to H atoms, suggesting that M-H interactions exhibit charge-transfer characteristics and ionic components[39]. Based on the above understanding, the results of this study can be interpreted from the perspective of electronegativity differences: a larger EDV_{alloy} corresponds to a stronger trend of charge transfer from the metal to H and a stronger average M-H interaction, making H more stable at the interstitial sites, thus resulting in a higher ΔH_{des}. Conversely, when EDV_{alloy} decreases, the alloy's average

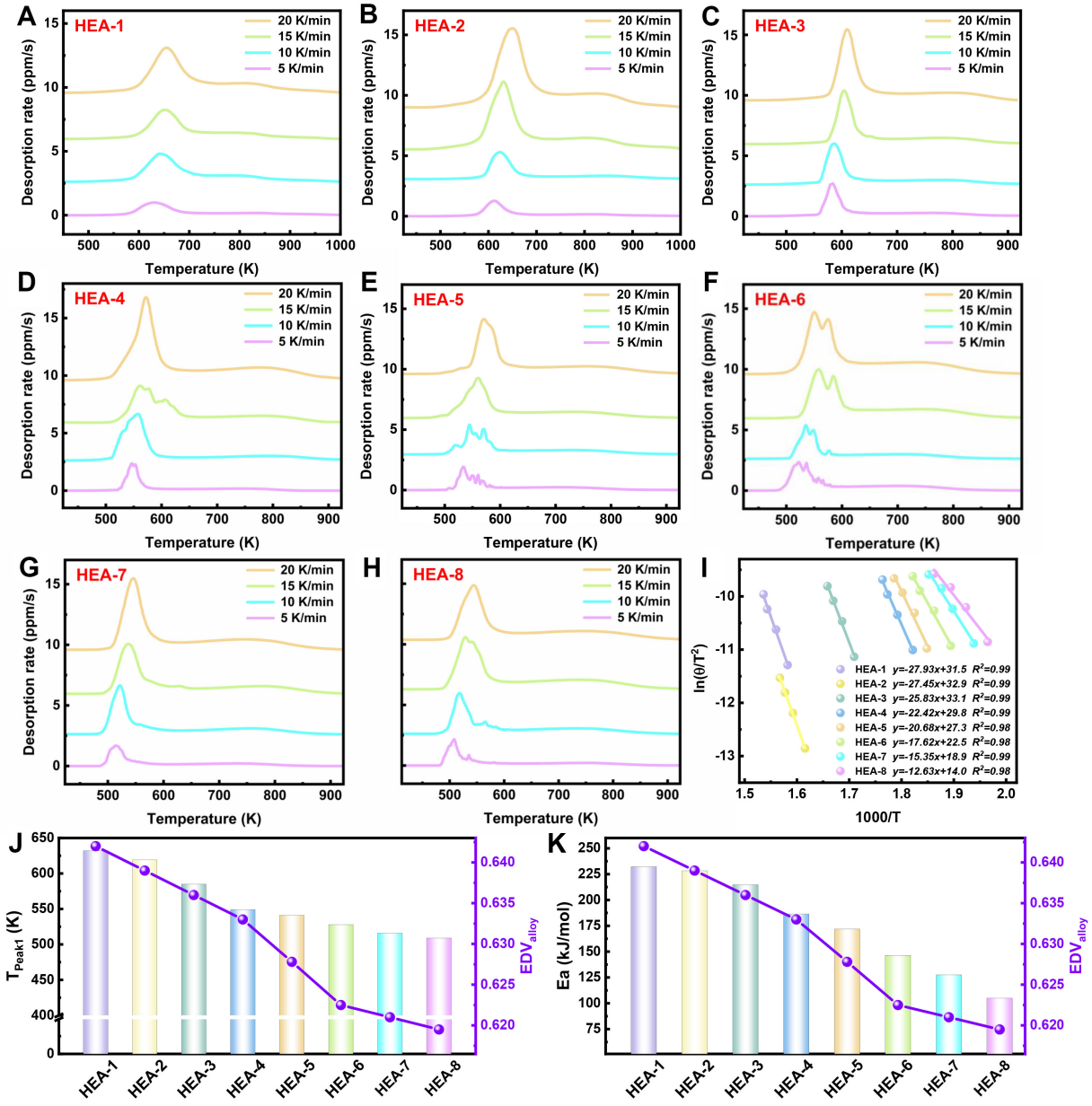

Figure 11. TDS curves for HEA-1 to HEA-8 alloys at different heating rates (5, 10, 15, 20 K/min) (A-H), corresponding Kissinger fitting results (I), the correlation between hydrogen release temperature and EDV_{alloy} (J), and the relationship between E_a and EDV_{alloy} (K). The TDS curves in (A-H) are vertically offset for clarity. HEA: High-entropy alloy; EDV_{alloy}: electronegativity difference value of the alloy; TDS: thermal desorption spectroscopy.

electronegativity approaches that of H, the average charge-transfer driving force may weaken, and the M-H bond strength decreases accordingly, thereby reducing the energy required for hydride decomposition.

It should be noted that EDV_{alloy} is an average composition descriptor whose validity depends on a single-phase BCC structure and a relatively uniform elemental distribution. For alloy systems containing a second phase, significant segregation, or complex multi-phase reactions, local hydrogen-occupancy environments and hydrogen absorption/desorption reactions involving the second phase may weaken the correlation between EDV_{alloy} and ΔH_{des}. Therefore, EDV_{alloy} is more suitable as an effective empirical descriptor for regulating the thermodynamic stability of hydrogen desorption in single-phase BCC hydrogen storage HEAs, rather than as the sole parameter independently determining all hydrogen storage behavior.

Microscopic dehydrogenation behavior regulated by EDV_{alloy}

The decrease in ΔH_{des} indicates a decline in the overall thermodynamic stability of the hydride; however, it is difficult to determine which stage of the dehydrogenation process EDV_{alloy} affects solely from a Van't Hoff analysis. Based on the aforementioned multi-peak characteristics observed in the TDS and XRD analyses of samples with different hydrogen contents, it can be concluded that the dehydrogenation process of TiVZrNb-based alloys is not a single-step reaction. Specifically, hydrogen-rich FCC dihydrides first decompose and transform into BCC-type intermediate hydrides; subsequently, the intermediate hydrides undergo further dehydrogenation, ultimately reverting to a low-hydrogen BCC solid solution or the initial BCC alloy structure. Therefore, the different dehydrogenation peaks in the TDS do not merely reflect hydrogen released at different temperatures, but rather correspond to the gradual release of hydrogen from different hydride phases, hydrogen occupation states, or local binding strengths. As EDV_{alloy} decreases, the main dehydrogenation peaks shift toward lower temperatures overall, indicating that the stability of hydrogen-rich hydrides and some intermediate hydrides is weakened. In particular, the low-temperature dehydrogenation peaks are relatively sensitive to changes in EDV_{alloy}, suggesting that electronegativity-driven regulation primarily acts on the hydrogen-rich dihydride phase. In this phase, H atoms extensively occupy interstitial sites in the metal lattice, and M-H interactions significantly contribute to the stability of the hydrides. As EDV_{alloy} decreases, the average M-H bond strength weakens, and the ability of FCC hydrides to maintain a high hydrogen content declines, increasing the likelihood of decomposition at lower temperatures. From a microscopic perspective, the hydrogen occupancy environment in high-entropy alloys exhibits significant diversity. Even when the alloy as a whole consists of a single-phase BCC solid solution, the coordination environments of Ti, V, Zr, and Nb around different interstitial sites vary, leading to a distribution of local M-H bond strengths and hydrogen-occupancy stabilities. A decrease in EDV_{alloy} does not imply that all local M-H bonds weaken proportionally; rather, it is more likely to manifest as a shift in the overall distribution of hydrogen binding energies toward lower stability. Specifically, this involves a reduction in the proportion of strongly bound H sites or a decrease in H stability in Ti/Zr-rich local environments. This overall decline in local stability can explain why the TDS main peak temperature shifts toward lower values as EDV_{alloy} decreases.

Furthermore, some high-temperature dehydrogenation peaks exhibit a relatively weak response to EDV_{alloy}, suggesting that this stage may be governed not only by average M-H bonding but also by factors such as residual hydrogen in low-hydrogen BCC solid solutions, the local interstitial environment, H diffusion pathways, lattice contraction, and defect confinement. Consequently, the influence of EDV_{alloy} on dehydrogenation pathways exhibits phase selectivity: it is more sensitive to the decomposition processes of hydrogen-rich hydrides and major intermediate hydrides, while local structural factors may limit its ability to describe low-hydrogen residual states.

Thermodynamic and kinetic effects of EDV_{alloy}

Both thermodynamic and kinetic factors govern the hydrogen release process. As the EDV_{alloy} content decreases, the alloy's ΔH_{des} drops significantly, indicating reduced thermodynamic stability of the hydride and making the hydrogen release reaction thermodynamically more favorable. Concurrently, the main dehydrogenation peak in the TDS curve shifts toward lower temperatures, and the apparent activation energy for the decomposition of hydrogen-rich dihydrides obtained from the Kissinger fit also decreases. This indicates that the reduction in EDV_{alloy} not only weakens the equilibrium stability of the hydrides but also reduces the kinetic resistance during the actual dehydrogenation process.

This simultaneous thermodynamic and kinetic change may stem from the weakening of the average M-H interaction. When EDV_{alloy} is high, the average electronegativity difference between the alloy and H is large, the driving force for electron transfer from the metal to H is strong, and H atoms are more strongly bound

by M-H bonding at interstitial sites. Consequently, hydride decomposition requires overcoming a larger thermodynamic energy difference, reflected in a higher ΔH_{des}; simultaneously, when H atoms detach from their local coordination environment to participate in subsequent diffusion, phase transition, and desorption processes, they must also overcome a higher energy barrier, reflected in a higher E_a. When EDV_{alloy} is reduced, the alloy's average electronegativity becomes closer to that of H, the average charge transfer driving force weakens, and the M-H bond strength decreases, reducing the stability of H atoms in hydrogen-rich hydrides. Consequently, the heat required for hydride decomposition decreases, and the combined kinetic energy barrier that must be overcome for H to escape interstitial sites and for the hydrogen-rich phase to decompose decreases as well.

From the perspective of dehydrogenation pathways, the decrease in E_a primarily reflects the improved kinetics of the decomposition process of the hydrogen-rich dihydride. In hydrogen-rich FCC dihydrides, the high hydrogen content causes H atoms to occupy a large number of interstitial sites in the metal lattice, making their stability highly sensitive to M-H interactions. When EDV_{alloy} decreases, the local confinement of H in the hydrogen-rich phase weakens, making it easier for the FCC dihydride to transform into intermediate hydrides or low-hydrogen BCC solid solutions. Consequently, the low-temperature dehydrogenation peak in the TDS shifts toward lower temperatures, and the corresponding apparent activation energy decreases. This indicates that the reduction in EDV_{alloy} not only lowers the thermodynamic stability of hydrogen-rich hydrides but also reduces the kinetic resistance to their decomposition and phase transformation.

CONCLUSION

In this study, based on the EDV_{alloy}, we designed and prepared TiVZrNb-based BCC hydrogen storage HEAs. We systematically investigated their phase structure, hydrogen storage capacity, hydrogen release thermodynamics, and dehydrogenation kinetics. The main conclusions are as follows:

(1) EDV_{alloy} shows a clearer correlation with ΔH_{des} than VEC, lattice parameters, and δ do for single-phase BCC hydrogen storage HEAs, indicating that EDV_{alloy} is more suitable as a first-order empirical descriptor for describing the variation trend of hydride stability in BCC hydrogen storage HEAs, rather than as the only parameter that completely replaces lattice structure, compositional effects, and electronic-structure factors.

(2) By reducing the Ti/Zr content and increasing the Nb content, the EDV_{alloy} of the HEA-1 to HEA-8 alloys decreased from 0.6420 to 0.6195. All alloys maintained a compositionally homogeneous single-phase BCC structure and exhibited high hydrogen storage capacities approaching H/M = 2, indicating that this compositional control strategy did not compromise the alloys' phase stability or high-capacity hydrogen storage characteristics.

(3) As EDV_{alloy} decreased, the alloy's ΔH_{des} decreased from 230.3 kJ/mol H_2 to 97.3 kJ/mol H_2, and the main dehydrogenation peak shifted to lower temperatures. This indicates that reducing the average electronegativity difference between the alloy and hydrogen weakens M-H interactions, thereby destabilizing hydrogen-rich hydrides thermodynamically.

(4) TDS, structural analysis of samples with different hydrogen contents, and Kissinger analysis indicate that the reduction in EDV_{alloy} primarily affects the dehydrogenation behavior of hydrogen-rich FCC dihydrides and certain BCC intermediate hydride phases, while also lowering the apparent activation energy of the hydrogen-rich dihydride decomposition process. This suggests that it not only reduces the thermodynamic stability of the hydrides but also decreases the kinetic resistance of the main dehydrogenation stages. The above results provide an effective design strategy for reducing the stability of hydrides in TiVZrNb-based

BCC hydrogen storage HEAs while maintaining high hydrogen storage capacity.

DECLARATIONS

Authors' contributions

Investigation: Zha, L.; Liu, L; Wang, Y.; Cai, H.; Zhang, Y.; Du, H.
Data curation: Zha, L.; Liu, L; Wang, Y.; Cai, H.; Zhang, Y.; Du, H.; Dou, B.; Xue, L.; Zhao, Y.
Formal analysis: Zha, L.
Writing - original draft: Zha, L.
Methodology: Dou, B.; Xue, L.; Zhao, Y.; Wan, D.
Conceptualization: Dou, B.; Xue, L.; Zhao, Y.; Wan, D.; Xue, Y.
Writing - review & editing: Wan, D.
Visualization: Wan, D.
Validation: Wan, D.; Xue, Y.
Resources: Wan, D.; Xue, Y.
Project administration: Wan, D.; Xue, Y.
Supervision: Xue, Y.
Funding acquisition: Xue, Y.

Availability of data and materials

The data supporting the findings of this study are available within this Article and its Supplementary Materials. Further data are available from the corresponding authors upon request.

AI and AI-assisted tools statement

Not applicable.

Financial support and sponsorship

This work is supported by the National Natural Science Foundation of China (Grant No. 52301128) and the Fundamental Research Funds for the Central Universities, Beijing Institute of Technology (Grant No. XSQD-6120220309).

Conflicts of interest

All authors declared that there are no conflicts of interest.

Ethical approval and consent to participate

Not applicable.

Consent for publication

Not applicable.

Supplementary Materials

Supplementary Materials

REFERENCES

1. Lenis, J. A.; Arias, Velandia. J.; Aguirre, Ocampo. R.; et al. Challenges and potential future trends on high entropy alloy for solid hydrogen storage: systematic review. *J. Power. Sources.* **2025**, *656*, 238011. DOI
2. Allendorf, M. D.; Stavila, V.; Snider, J. L.; et al. Challenges to developing materials for the transport and storage of hydrogen. *Nat. Chem.* **2022**, *14*, 1214-23. DOI
3. Paul, A. R.; Mehla, S.; Bhargava, S. Intermetallic compounds for hydrogen storage: current status and future perspectives. *Small* **2025**, *21*, e2408889. DOI PubMed

4. Gao, S.; Qi, J.; Jia, K.; Zhang, L.; Wu, F.; Xiao, X. A review of high-entropy alloys for next-generation solid-state advanced hydrogen storage materials. *Compos. Pt. B-Eng.* **2026**, *312*, 113340. DOI
5. Liu, J.; Huang, P.; Xia, Y.; et al. High-entropy alloys for hydrogen storage, separation, and detection: Recent progress and prospects. *eScience* **2026**, *6*, 100506. DOI
6. Luo, L.; Chen, L.; Li, L.; et al. High-entropy alloys for solid hydrogen storage: a review. *Int. J. Hydrog. Energy.* **2024**, *50*, 406-30. DOI
7. Ramatsoma, B.; Makhatha, M.; Klenam, D.; Bodunrin, M. Role of compositionally complex and high entropy alloys for hydrogen storage: a bibliometric and mechanistic assessment. *Renew. Sust. Energ. Rev.* **2025**, *222*, 115903. DOI
8. Amiri, A.; Shahbazian-Yassar, R. Recent progress of high-entropy materials for energy storage and conversion. *J. Mater. Chem. A.* **2021**, *9*, 782-823. DOI
9. Hu, H.; Zhang, X.; Li, S.; Yi, L.; Chen, Q. A review of body-centered cubic-structured alloys for hydrogen storage: composition, structure, and properties. *Rare. Metals.* **2025**, *44*, 1497-521. DOI
10. Halpren, E.; Yao, X.; Chen, Z. W.; Singh, C. V. Machine learning assisted design of BCC high entropy alloys for room temperature hydrogen storage. *Acta. Mater.* **2024**, *270*, 119841. DOI
11. Shen, S.; Li, Y.; Ouyang, L.; Zhang, L.; Zhu, M.; Liu, Z. V-Ti-based solid solution alloys for solid-state hydrogen storage. *Nanomicro. Lett.* **2025**, *17*, 175. DOI PubMed PMC
12. Bouzidi, A. Hydrogen absorption properties in high entropy alloys containing refractory elements, Université Paris-Est Créteil Val-de-Marne-Paris 12, 2023. Available from: https://hal.science/tel-04671333.
13. Greaves, F.; Bouzidi, A.; Perrière, L.; et al. Hydrogen induced phase transition in $TiZrNbHfV_{1-x}Ta_x$ high entropy alloys. *J. Phys. Chem. C.* **2025**, *129*, 2904-12. DOI
14. Bouzidi, A.; Laversenne, L.; Nassif, V.; Elkaim, E.; Zlotea, C. Hydrogen storage properties of a new Ti-V-Cr-Zr-Nb high entropy alloy. *Hydrogen* **2022**, *3*, 270-84. DOI
15. Montero, J.; Ek, G.; Laversenne, L.; Nassif, V.; Sahlberg, M.; Zlotea, C. How 10 at% Al addition in the Ti-V-Zr-Nb high-entropy alloy changes hydrogen sorption properties. *Molecules* **2021**, *26*, 2470. DOI PubMed PMC
16. Montero, J.; Zlotea, C.; Ek, G.; Crivello, J. C.; Laversenne, L.; Sahlberg, M. TiVZrNb multi-principal-element alloy: synthesis optimization, structural, and hydrogen sorption properties. *Molecules* **2019**, *24*, 2799. DOI PubMed PMC
17. Bouzidi, A.; Laversenne, L.; Zepon, G.; Vaughan, G.; Nassif, V.; Zlotea, C. Hydrogen sorption properties of a novel refractory Ti-V-Zr-Nb-Mo high entropy alloy. *Hydrogen* **2021**, *2*, 399-413. DOI
18. Agafonov, A.; Greaves, F.; Perrière, L.; Nassif, V.; Zlotea, C. Effective destabilization of both mono- and dihydride phases in TiVZrNbHf by Mo addition. *Scripta. Materialia.* **2026**, *275*, 117161. DOI
19. Mayer, G. C.; Silva, B. H.; Botta, W. J.; Zepon, G. Effect of cycling conditions on hydride stability of the $Ti_{11}Nb_{61}Cr_{28}$ alloy. *J. Mater. Chem. A.* **2026**, *14*, 7596-607. DOI
20. Nygård, M. M.; Ek, G.; Karlsson, D.; Sørby, M. H.; Sahlberg, M.; Hauback, B. C. Counting electrons - a new approach to tailor the hydrogen sorption properties of high-entropy alloys. *Acta. Mater.* **2019**, *175*, 121-9. DOI
21. Zhai, Y.; Li, Y.; Wei, S.; Tolj, I.; Kennedy, J.; Yang, F. Progress in V-BCC based solid solution hydrogen storage alloys. *J. Energy. Storage.* **2025**, *109*, 115103. DOI
22. Cai, H.; Zhang, Y.; Wang, H.; Wan, D.; Zhao, Y.; Xue, Y. Trace Nb and Mn regulation of hydrogen storage capacity and cyclic stability of BCC-type TiCrMo alloys. *ACS. Appl. Energy. Mater.* **2026**, *9*, 1834-44. DOI
23. Guo, S.; Ng, C.; Lu, J.; Liu, C. T. Effect of valence electron concentration on stability of fcc or bcc phase in high entropy alloys. *J. Appl. Phys.* **2011**, *109*, 103505. DOI
24. Guo, S.; Liu, C. Phase stability in high entropy alloys: formation of solid-solution phase or amorphous phase. *Prog. Nat. Sci.* **2011**, *21*, 433-46. DOI
25. Zhang, Y.; Zhou, Y.; Lin, J.; Chen, G.; Liaw, P. Solid-solution phase formation rules for multi-component alloys. *Adv. Eng. Mater.* **2008**, *10*, 534-8. DOI
26. Yang, X.; Zhang, Y. Prediction of high-entropy stabilized solid-solution in multi-component alloys. *Mater. Chem. Phys.* **2012**, *132*, 233-8. DOI
27. Westlake, D. Stabilities, stoichiometries and site occupancies in hydrides of intermetallic compounds. In: Electronic structure and properties of hydrogen in metals; Springer, 1983; pp 85-96. DOI
28. Somo, T. R.; Lototskyy, M. V.; Yartys, V. A.; Davids, M. W.; Nyamsi, S. N. Hydrogen storage behaviours of high entropy alloys: a review. *J. Energy. Storage.* **2023**, *73*, 108969. DOI
29. Jiang, M.; Song, A.; Yan, Y.; Feng, W.; Li, H.; Liang, B. Applicability and limitations of hydrogen affinity as a descriptor for designing high-entropy alloys for hydrogen storage. *Chem. Mater.* **2026**, *38*, 3666-75. DOI
30. Jang, S. H.; Zhang, D.; Tran, H. B.; et al. Physically interpretable descriptors drive the materials design of metal hydrides for hydrogen storage. *Chem. Sci.* **2025**, *16*, 23111-20. DOI PubMed PMC

31. Metal-hydrogen system under extended *p*, *T* conditions. In Fukai, Y., editor. The metal-hydrogen system: basic bulk properties; Springer Berlin Heidelberg, 2005; pp 91-145. DOI
32. Somo, T. R. High entropy hydrogen storage alloys and perspectives of their application in hydrogen storage systems operating at near-ambient temperatures. University of the Western Cape, 2024. https://hdl.handle.net/10566/21454.
33. Zlotea, C.; Bouzidi, A.; Montero, J.; Ek, G.; Sahlberg, M. Compositional effects on the hydrogen storage properties in a series of refractory high entropy alloys. *Front. Energy. Res.* **2022**, *10*, 991447. DOI
34. Ponsoni, J. B.; Aranda, V.; Nascimento, T. D. S.; Strozi, R. B.; Botta, W. J.; Zepon, G. Design of multicomponent alloys with C14 laves phase structure for hydrogen storage assisted by computational thermodynamic. *Acta. Mater.* **2022**, *240*, 118317. DOI
35. Chen, K.; Lau, M. Y.; Luo, X.; Huang, J.; Ouyang, L.; Yang, X. Research progress in solid-state hydrogen storage alloys: a review. *J. Mater. Sci. Technol.* **2026**, *246*, 256-89. DOI
36. Suarez-Alcantara, K.; Torres-Garcia, N. L.; del, Carmen. Cintron-Nuñez. P. HEAs with Ti - V - Zr for hydrogen storage, a verification of the predictability of VEC (valence electron concentration) and electronegativity difference over the hydriding temperature. *J. Alloy. Compd.* **2025**, *1046*, 184794. DOI
37. Hassan, N. O.; Ghais, A.; Ahmed, M. H.; et al. Density functional theory insights into the structure, electronic and mechanical properties, thermodynamics, and diffusion of high-entropy alloys for hydrogen storage: a review. *Int. J. Hydrog. Energy.* **2026**, *217*, 153928. DOI
38. Matumura, T.; Yukawa, H.; Morinaga, M. Alloying effects on the electronic structures of VH_2 and V_2H. *J. Alloy. Compd.* **1999**, *284*, 82-8. DOI
39. Hu, J.; Li, X.; Vitos, L.; Schönecker, S. Effects of Mg and Al doping on the desorption energetics and electronic structure of a Ti-V-Zr-Nb alloy hydride. *Acta. Mater.* **2024**, *277*, 120198. DOI
40. Pauling, L. The nature of the chemical bond - 1992. *J. Chem. Educ.* **1992**, *69*, 519. DOI
41. Cheng, B.; Kong, L.; Li, Y.; Wan, D.; Xue, Y. Hydrogen desorption kinetics of $V_{30}Nb_{10}(Ti_xCr_{1-x})60$ high-entropy alloys. *Metals* **2023**, *13*, 230. DOI
42. Cheng, B.; Dou, B.; Kong, L.; Wan, D.; Xue, Y. Synergistic and competing effects of iron in TiVNbCr-based high-entropy alloys for reversible hydrogen storage. *Small* **2025**, *21*, e08310. DOI PubMed
43. Cheng, B.; Kong, L.; Cai, H.; et al. Pushing the boundaries of solid-state hydrogen storage: a refined study on TiVNbCrMo high-entropy alloys. *Int. J. Hydrog. Energy.* **2024**, *60*, 282-92. DOI
44. Cai, H.; Dou, B.; Xue, L.; et al. Engineering Ti-Cr-Mo-based alloys for hydrogen storage: Fe doping as a strategy for improved reversibility and stability. *Int. J. Hydrog. Energy.* **2025**, *128*, 499-510. DOI
45. Huang, Z.; Li, C.; Chu, Y.; et al. Potential and challenges for V-based solid solution hydrogen storage alloys. *Energy* **2025**, *316*, 134574. DOI
46. Sandrock, G. A panoramic overview of hydrogen storage alloys from a gas reaction point of view. *J. Alloy. Compd.* **1999**, *293-295*, 877-88. DOI
47. Esayed, A. The use of the half cycle technique to examine hysteresis in $Zr(FexCr_{1-x})_2$ (x = 0.55 and 0.75) - H systems. *Int. J. Hydrog. Energy.* **2000**, *25*, 151-6. DOI
48. Weadock, N. J.; Voorhees, P. W.; Fultz, B. Interface pinning causes the hysteresis of the hydride transformation in binary metal hydrides. *Phys. Rev. Materials.* **2021**, *5*, 013604. DOI
49. Nygård, M. M.; Ek, G.; Karlsson, D.; Sahlberg, M.; Sørby, M. H.; Hauback, B. C. Hydrogen storage in high-entropy alloys with varying degree of local lattice strain. *Int. J. Hydrog. Energy.* **2019**, *44*, 29140-9. DOI
50. Montero, J.; Ek, G.; Laversenne, L.; et al. Hydrogen storage properties of the refractory Ti-V-Zr-Nb-Ta multi-principal element alloy. *J. Alloy. Compd.* **2020**, *835*, 155376. DOI